NBSIR 87-3081

DEVELOPMENT OF NEAR-FIELD TEST PROCEDURES FOR COMMUNICATION SATELLITE ANTENNAS PHASE 1, PART 2

Allen C. Newell

NBSIR 87-3081

DEVELOPMENT OF NEAR-FIELD TEST PROCEDURES FOR COMMUNICATION SATELLITE ANTENNAS PHASE 1, PART 2

Allen C. Newell

Electromagnetic Fields Division
Center for Electronics and Electrical Engineering
National Engineering Laboratory
National Bureau of Standards
Boulder, Colorado 80303-3328

CONTENTS

DEVELOPMENT OF NEAR-FIELD TEST PROCEDURES
FOR COMMUNICATION SATELLITE ANTENNAS
PHASE I, PART 2

Allen C. Newell

Electromagnetic Fields Division
National Bureau of Standards
Boulder, Colorado 80303

The purpose of this program is to define and further develop the
capabilities of near-field antenna test techniques, specifically
for the requirements associated with the development and
verification testing of reconfigurable, multibeam, frequency
reuse, commercial satellite antennas. This report, Phase I,
Part 2, focuses on the planar near-field measurement method and
covers the determination of sampling criteria and scan limits,
development of diagnostic and design assist methods, development
of beam alignment techniques, development of swept-frequency
equivalent tests, and specification of hardware requirements for
the measurement system. Phase I, Part 1, a previous report, gave
a general survey, definition, and description of near-field and
compact range measurement methods as they apply to satellite
antenna systems testing. Each of these methods was evaluated to
determine how well they meet the measurement requirements.
Included for each technique was a summary of the measurement
method, discussions on probe correction and data processing,
measurement hardware considerations, a results available section,
and measurement accuracy and range certification considerations.
The basis for the choice of the best measurement technique was
established with the planar near-field measurement method
receiving the best score for the directive antennas considered.
It is for this reason that the planar near-field method is the
focus of this report.

Key words: antenna alignment; antenna boresight measurements;
antenna diagnostics; antenna measurements; antennas; near-field
measurements; near-field testing; planar near-field scanning;
satellite antennas; swept-frequency measurements

1. Introduction

   The purpose of this program is to define and further develop the capabil-
ities of near-field antenna test techniques, specifically for the requirements
associated with the development and verification testing of reconfigurable,
multibeam, frequency reuse, commercial satellite antennas. The program in-
cludes two phases. Phase I was a study program that included the following
tasks as outlined in the statement of work:

Task I/A & I/I   General survey, definition, and description of near-field and
                  compact range configurations including a description of their
                  comparative advantages. These tasks were discussed in two
                  parts:

1.   A clear and concise description of the antenna and satellite
      systems to be measured, and the associated measurement problems.

2.   A description of the three near-field measurement techniques being
      studied along with the compact range approach. Each of these was
      evaluated to determine how well they met the requirements defined
      in Part 1 above.

Task I/H   Selection of the optimum measurement technique from the above
            study.

The results of the above tasks were reported in Phase I, Part 1 of the
final report, March 1985 [1]. Since the planar near-field method was chosen
as the optimum technique, the remainder of the study will focus on that
technique only. Items to be covered in the remainder of Phase I are:

Task I/B   Determination of sampling criteria and scan limits.

Task I/C   Development of diagnostic and design assist methods.

Task I/D   Development of beam alignment techniques.

Task I/E   Development of swept-frequency equivalent tests.

Task I/F   Specification of hardware requirements for the measurement system.

Task I/G   Outline available computer programs and make them available.

Task I/J   Develop the test plan for Phase II.

Tasks I/B, I/C, I/D, I/E and I/F are considered in this report, thereby
completing the final report for Phase I (Tasks I/G and I/J have been reported
separately).

Phase II is a measurement program that will demonstrate the results of
Phase I.

2

2. Development of Scan Limits for Planar Near-Field Measurements on
    Spacecraft Antennas in an "Antenna Farm" Environment

The consideration of scan limits in planar near-field measurements is
related to the calculation of the angular spectrum of the measured near-field
data.

$$D'(\underline{K}) = \frac{e^{-i\gamma d}}{4\pi^2 \; F'A'} \int\limits_{-\infty}^{\infty} \int\limits_{-\infty}^{\infty} B_0'(\underline{P}) \; e^{-i\underline{K}\cdot\underline{P}} \; dx \; dy \tag{1}$$

The notation employed here is the same as in Part I [1] [see appendix A,
eq (A54)], where $B_0'(\underline{P})$ represents the relative near-field data, and $D'(\underline{K})$ its
angular spectrum. The limits of integration in eq (1) are over an infinite
measurement plane. Whenever the plane is truncated to a realizable meas-
urement system, there is a loss of information; therefore errors arise in the
calculation of $D'(\underline{K})$. A number of studies related to these errors involving
theoretical analysis, computer simulation, and measurements have been carried
out. The result is that the effect of scan area truncation is well understood
and a variety of techniques are available to reliably predict its effect. In
the following section the results of the previous studies will be reviewed.
We will then consider to what extent they need to be modified for the
particular antenna types under consideration in this study.

The basic result of all the studies on truncation errors has been that
there are two distinct effects. First, the calculated spectrum, $D'(\underline{K})$ is
valid only within a limited angular region of the forward hemisphere; and
second, there are some errors even within this "angular region of validity."
The formulation of the first effect was derived originally from measurements
on a limited number of antennas [2] and was later derived analytically [3].
Subsequent to the early measurements, the result has been found to hold for a
wide variety of antennas, some of which are noted in table 1. The basic
result is illustrated in figure 1 and shows that the region of validity can be
determined from a very simple geometric relation.

Table 1. Sample of antennas measured on the NBS near-field facility.

Antenna type	Freq. (GHz)	Major dimension in wavelength	Gain (dB)
Horn lens	48.0	90	47.0
Conical horn (JPL)	8.0	6	22.08
Cassegrain reflector	60.0	91	46.5
Lens array (constrained lens)	9.2	23	34.0
Phased array (volphase)	8.4	17	21.5
Phased array	7.5	15	30.5
Dipole array	1.4	5	20.3
Fan beam radar (linear and circular polarization)	9.5	58	30.0
Ku-band reflector	14.5	60	42.0
Ku-band array (pencil and fan beam)	17.0	50	40.0
Shaped beam, C.P. (array fed reflector)	4.0	20	27.5
Microstrip array	1.5	27	30.0
Parabolic reflector	1.5-1.8	15-183	26-47
Compact range reflector	18 & 55	285 & 870	~60.0
Slotted waveguide array	3.0	60	30.0

Maximum Angle for Accurate Far Field $= \theta_s$

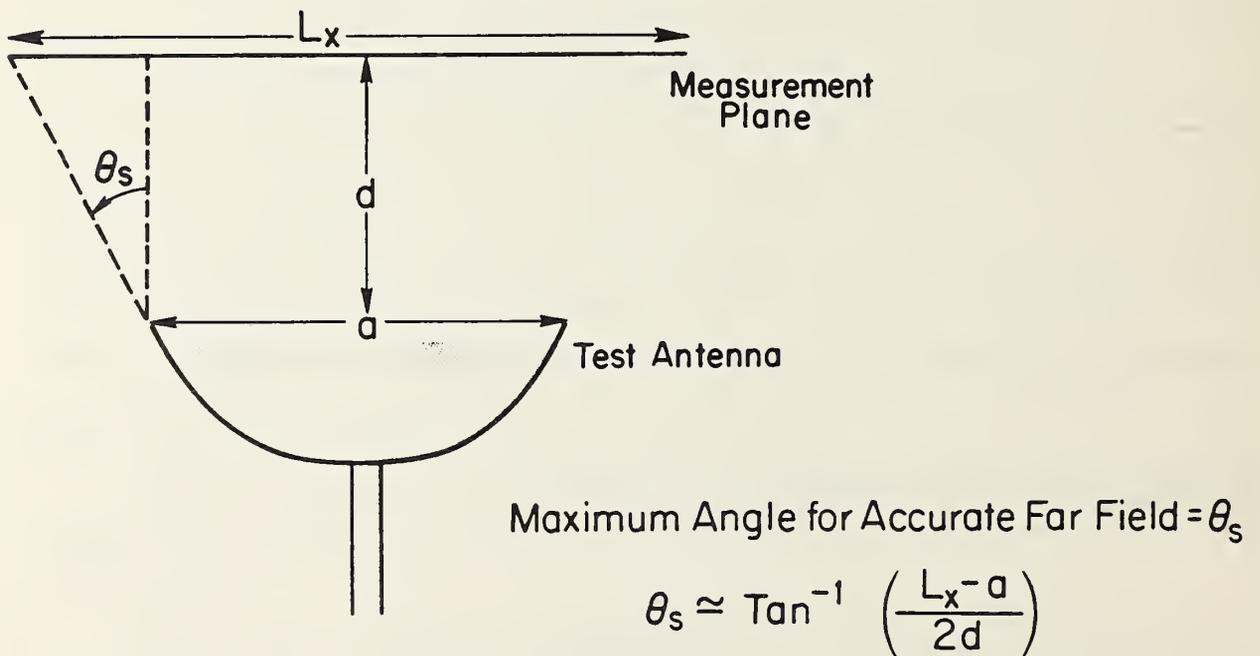$$\theta_s \simeq \mathrm{Tan}^{-1}\left(\frac{L_x - a}{2d}\right)$$

Figure 1. Relationship between scan area and region where results are valid.

4

The predicted region of validity has been confirmed for antennas very similar to the INTELSAT VI types. From near-field measurements on the engineering model of the INTELSAT IV A antenna, computer tests were performed to gradually reduce the size of the scan area and note the change in the resulting far-field pattern. As predicted by the equation in figure 1, the pattern results within the angle θ_S were virtually identical to results for larger scan areas, but as the scan area decreased, the pattern at the outer limits would systematically change.

The impact of this first effect on the satellite antenna testing was discussed in some detail in Part 1 [1] of the final report (see section 3.1.4). If the complete antenna farm of the Intelsat VI satellite is included, scan areas of up to 10.4 x 6.6 m may be required. While this is technically feasible, it may be more practical to limit the testing to each reflector and its feed. This requires a much smaller scanner and will still give very good results for each separate antenna. There are also alternate approaches that allow use of moderate size scanners for measurements over quite large scan areas. One technique that has been used successfully in a number of applications is represented schematically in figure 2. The antenna is mounted on a set of rails that run parallel to the scan plane and moved to a series of positions in front of the scanner. In each of these positions the antenna is precisely aligned and the scanner obtains a set of near-field data for each position. The data sets are then combined as illustrated in figure 3 to provide an effective scan area a number of times larger than the scanner. This technique could be used to study scattering effects over large areas, and then single sets over one scan area could be used in final testing of each antenna system.

This technique has been used to measure large arrays [4], and in another measurement facility [5] the antenna is always moved in one axis while the probe is moved in the orthogonal direction. The technique has therefore been tested and shown effective and reliable.

The second effect of scan area truncation is that it produces some errors in the pattern even within the region of validity. Equations to estimate the magnitude of these errors were first derived by Yaghjian [3]. He showed that this error can be estimated from a knowledge of the measured data on the boundary of the scan area even though the error results from neglecting all
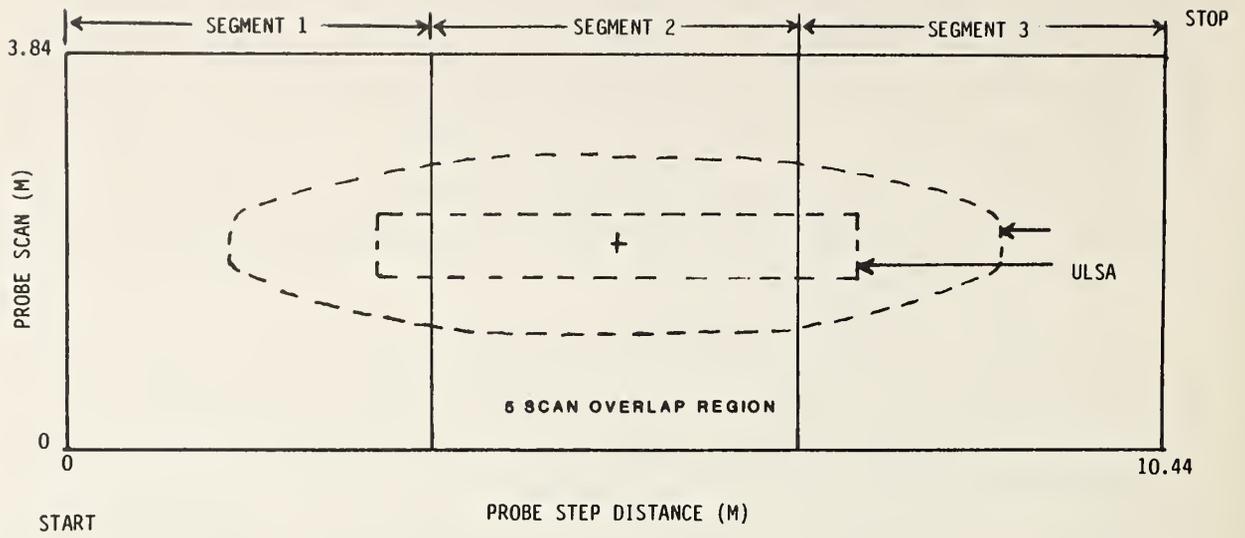
5

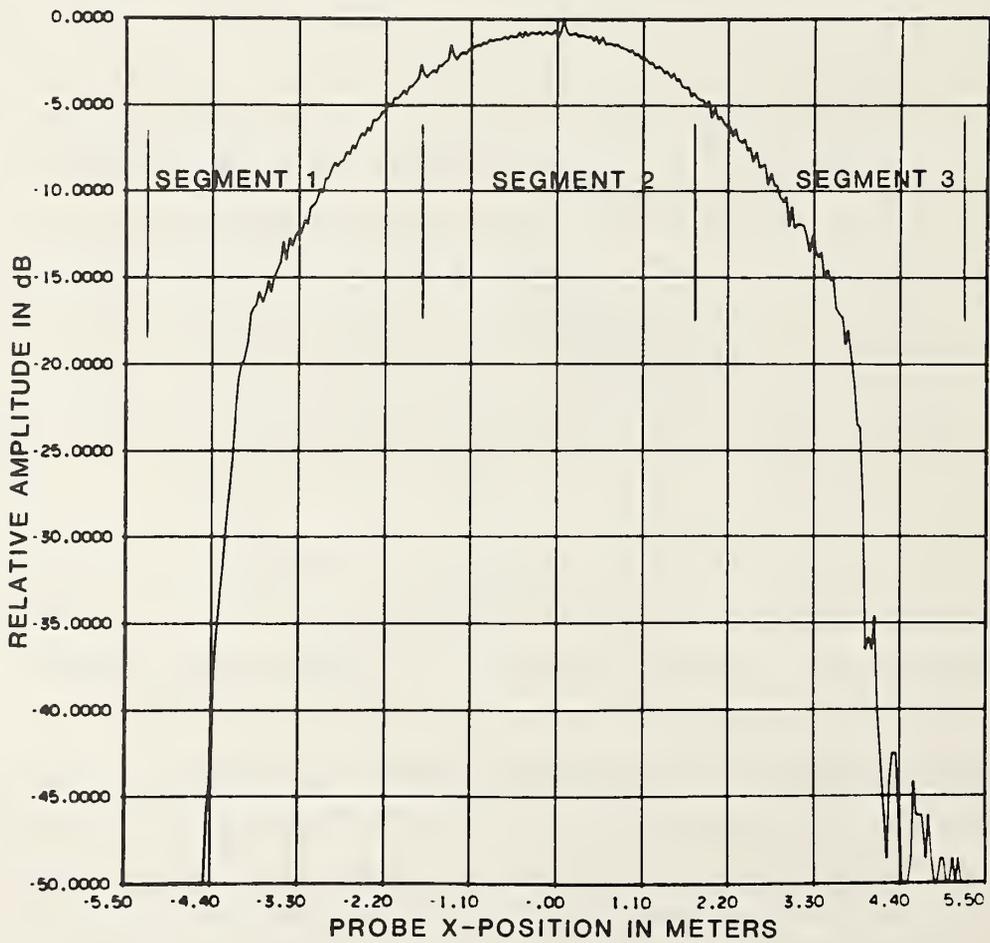Figure 2. Schematic for probing of large antennas by segmented scanning.

Figure 3. Composite data from three segments.

6

the data on the infinite plane outside the scan area. If we denote the plane polar coordinates of the boundary as (p', ϕ_p), the data within and on the boundary, respectively, as $B(\underline{P})$ and $B(p', \phi_p)$, and the spherical coordinates of the far-field directions by (θ, ϕ), then the fractional error in that direction is

$$\left| \frac{\Delta D(\theta, \phi)}{D(\theta, \phi)} \right| \leq \frac{\lambda \left| \int_0^{2\pi} B(p', \phi_p) e^{-ikp' \sin\theta \cos(\phi - \phi_p)} p' d\phi_p \right|}{2\pi \delta_x \delta_y \left| \sum B(\underline{P}) e^{-i\underline{K} \cdot \underline{P}} \right| \cos\gamma_{max}}. \tag{2}$$

In eq (2), γ_{max} is the maximum acute angle between the plane of the scan area and any line connecting the edges of the antenna aperture and the scan area, and

$$\underline{K} = k \sin\theta \cos\phi \; \underline{e}_x + k \sin\theta \sin\phi \; \underline{e}_y. \tag{3}$$

Equation (2) can be easily evaluated after complete measurements have been completed and $B(P', \phi_\rho)$ is known. If preliminary estimates of the truncation error are desired, another relation is available [3] requiring less information, but generally predicting much larger upper bound errors. This is

$$\left| \frac{\Delta D(\underline{K})}{D(\underline{K})} \right| \leq \frac{\alpha \lambda L_{max} B_{max}(p', \phi_\rho)}{2 \; A \cos \gamma_{max}} \; g(\underline{K}) \tag{4}$$

where A =   area of antenna aperture

     L_{max} = maximum width of scan area

     α = a taper factor (see discussion by Yaghjian in reference)
         $\alpha \approx 1 - 5$

     $g(\underline{K}) = \left| D(\underline{K}_0)/D(\underline{K}) \right|$ = ratio of peak pattern amplitude at $\underline{K}_0$ to the amplitude at $\underline{K}$.

The character of the truncation error can be seen clearly from the results of a computer simulation using the actual near-field data. In this program, the FFT is not used to evaluate the integral in eq (1); rather a direct summation is used so that the _path_ of integration can be chosen in a special way. First a single direction in the far-field corresponding to $\underline{K} = \underline{K}_0$ is chosen. For instance, if the on-axis direction along the Z-axis is desired, $\underline{K} = \underline{0}$ is used. Next, the integral of eq (1) is evaluated for this

7

value of $\underline{K}$, and the path of integration starts at the center of the measurement area and spirals out along the boundaries of the gradually increasing rectangular areas shown in figure 4. The result of this evaluation for a sample antenna and for $\underline{K} = \underline{0}$ corresponding to the peak of the main beam is shown in figure 5. When the integration area is less than the projected area of the antenna, the results may vary over a wide range. As the size of the integration rectangle approaches the value where θ_s of figure 1 is equal to the direction to the sidelobe under consideration, the integral begins to converge to a relatively constant value. There are, however, some oscillations in the computed value of $D(\underline{K})$ as the area is increased, and these oscillations represent the effect of the truncation error. For comparison, the error bounds as predicted by eqs (2) and (4) are also shown on figure 5, showing that they do indeed give realistic upper bound estimates of the effect of truncation.

Another way of estimating the effect of truncation involves the use of eq (2) and the actual measured data to calculate an effective error spectrum resulting from the finite scan area. This error spectrum is obtained by calculating the Fourier transform of the measured data with all measured amplitudes not on the boundary set to zero. This spectrum is basically the numerator of eq (2) and represents an upper bound estimate of the error spectrum produced by truncation.

An example of this test is shown in figures 6 through 8. Figure 6 is a perspective plot of the measured near-field amplitude for a sample antenna, and figure 7 the far-field spectrum resulting from the combined amplitude and phase. Figure 8 is then the spectrum for the same far-field directions when only the boundary points are used, indicating that for the scan area utilized truncation errors are negligible. Similar results can be obtained for any portion of the far-field.

One other approach is also useful for estimating the effect of truncation, and is often used in the initial phases of a measurement to determine the required size of the scan plane. This is the use of one-dimensional, centerline measurements data. Typically, these measurements are near or along the lines x = 0 and y = 0, or along regions of highest amplitude. Computer programs have been developed to compute the Fourier transforms of the one-dimensional data for the complete data sets and for partial data sets with

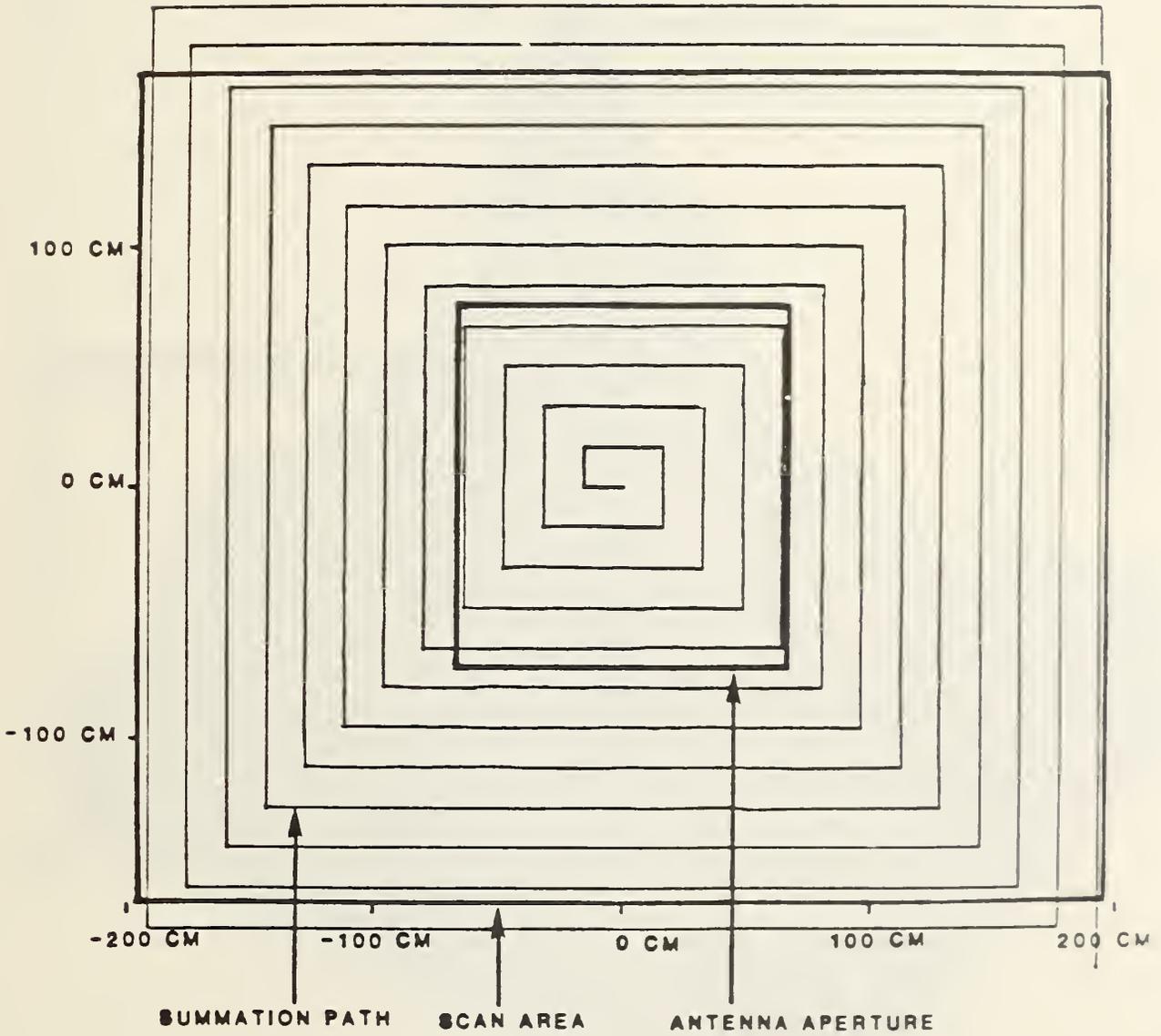Figure 4. Rectangular spiral path of integration used in truncation study.
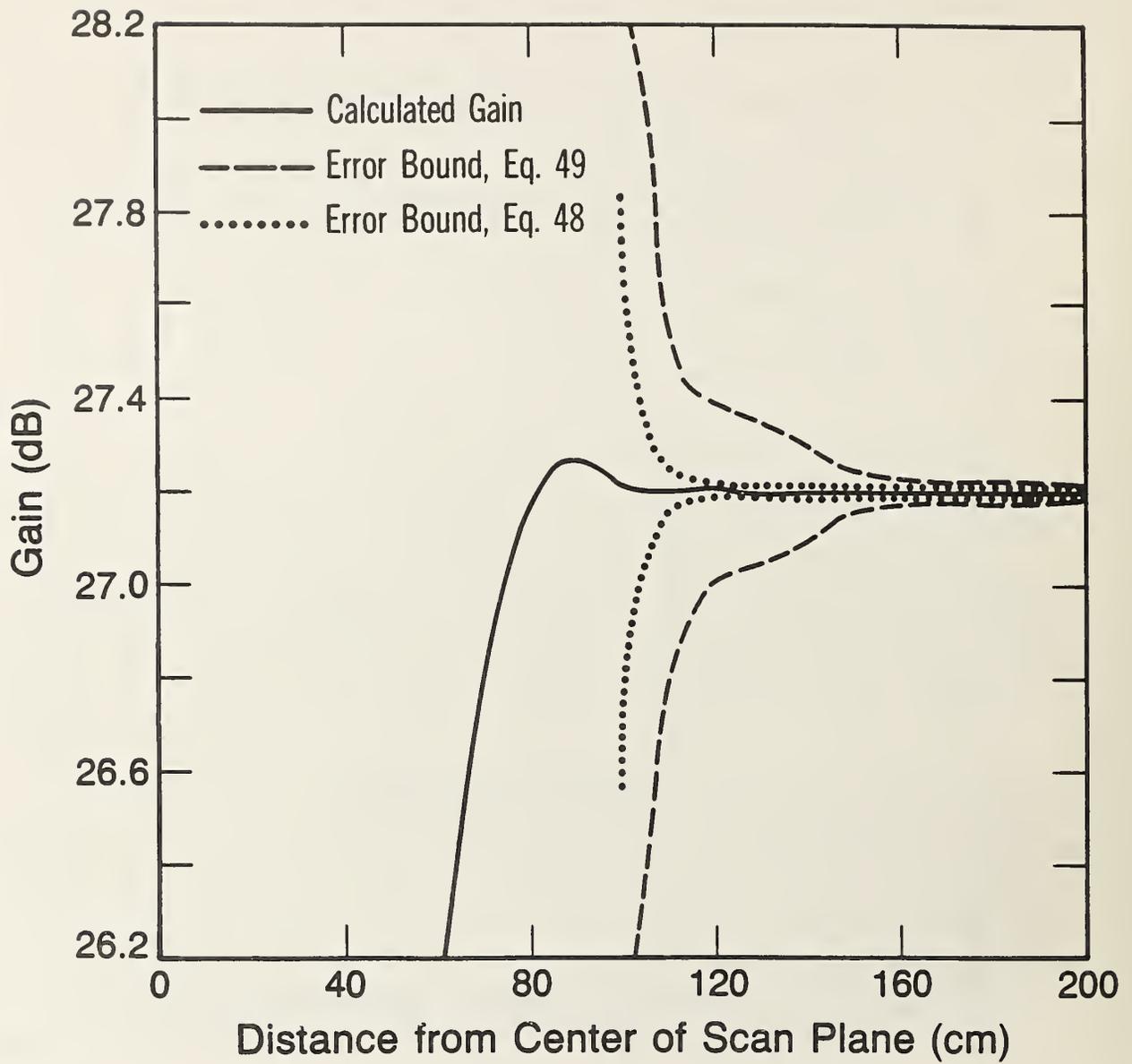
Figure 5. Results of truncation simulation study for Intelsat IV A antenna.
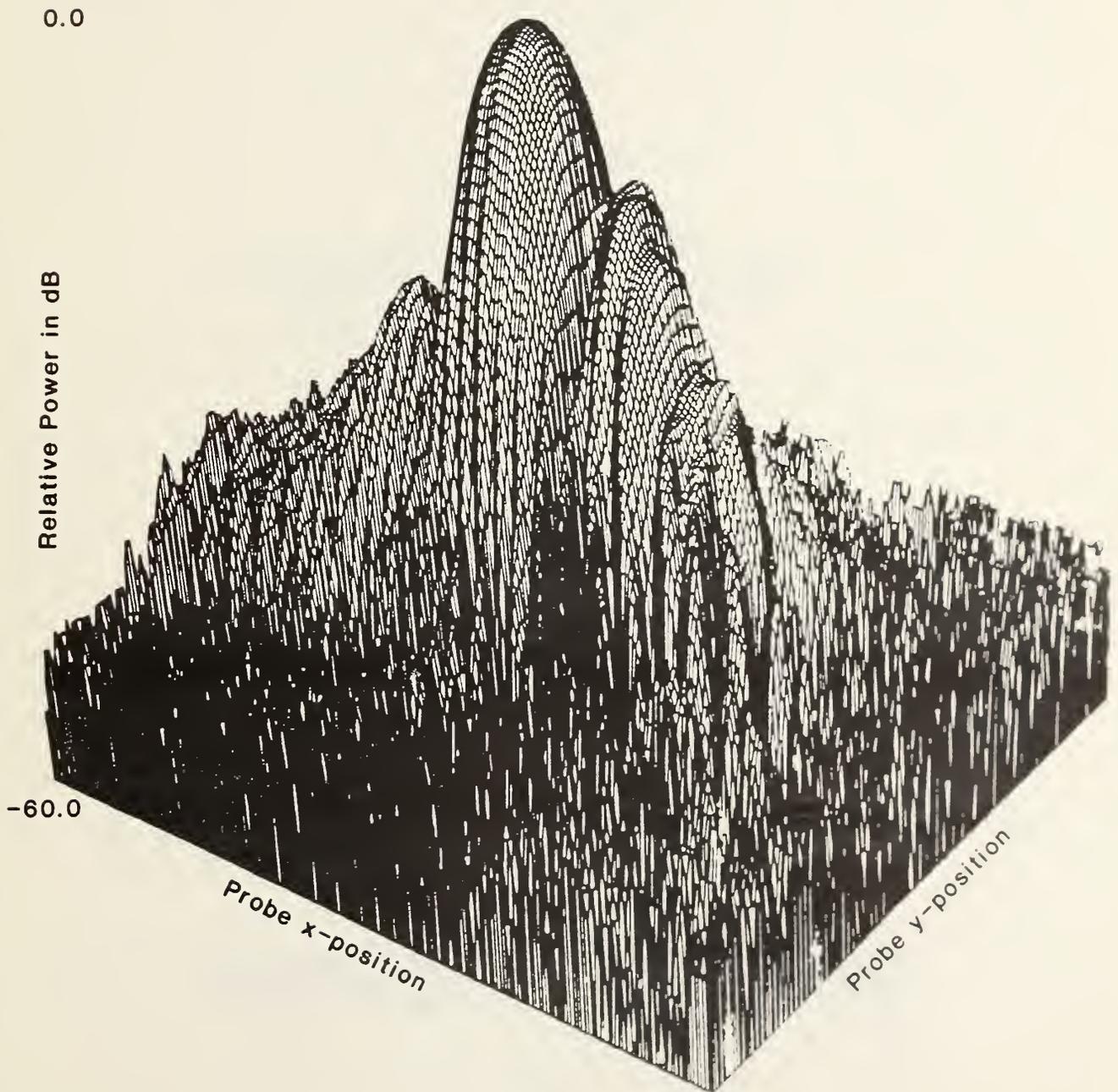
0.0

Relative Power in dB

-60.0

Probe x-position

Probe y-position

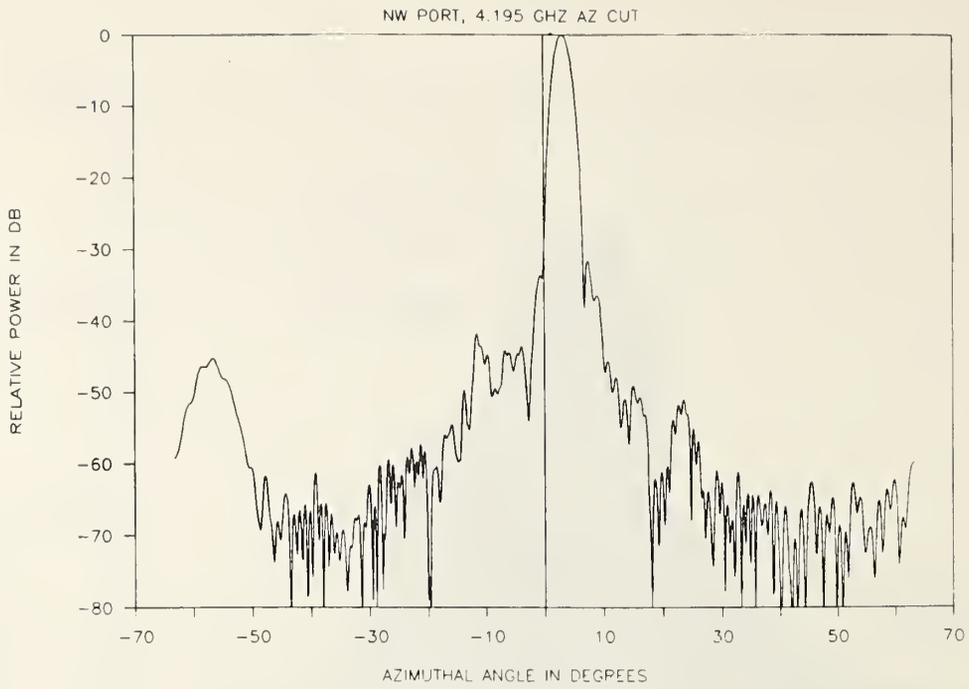Figure 6. Near-field amplitude on complete measurement plane.

11

Figure 7. Far-field spectrum in principal plane.
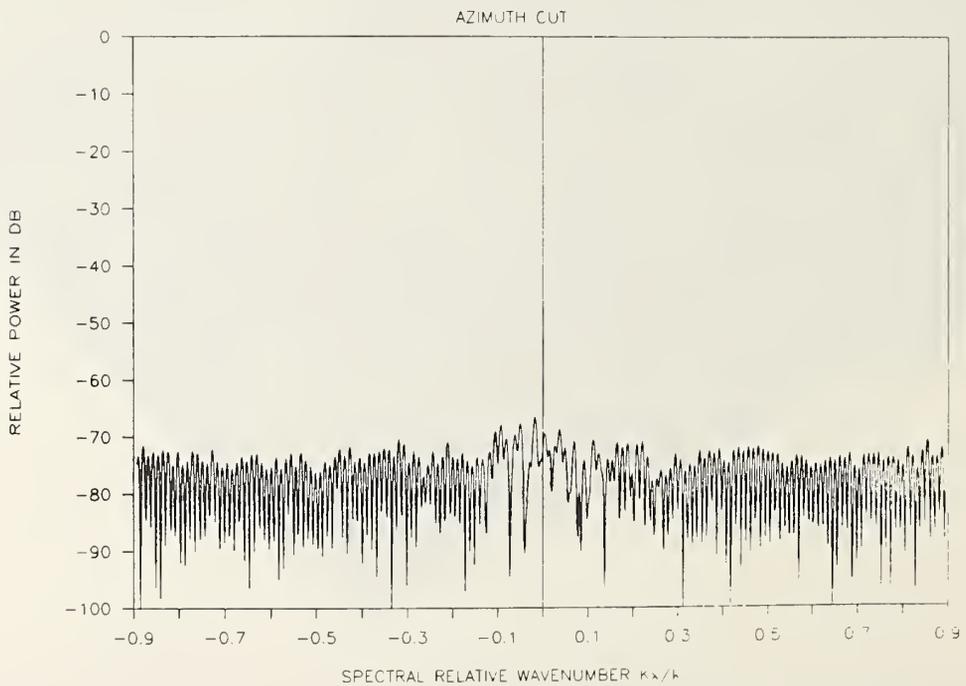
Figure 8. Error spectrum due to area truncation.

12

varying amounts of edge data deleted. These one-dimensional transforms are an approximation to the actual far field, and the change resulting from edge deletion is generally indicative of the change that will result from truncation in two dimensional scans. It is an approximate technique, but one that is useful in the initial set up of a measurement.

In summary, then, there are a number of techniques available to predict or estimate the error due to scan area truncation. In a sense they are similar to the techniques for estimating the effect of other sources of error. That is, as the information about the error increases, the error bound of the effect on the far-field becomes smaller. Listed in order of increasing information, and generally decreasing error bounds, they are:

A. Given the geometry of the measurement plane and antenna, the region of validity is determined.

B. With the maximum amplitude at the edge of the scan area and eq (4) a conservative upper bound error on far-field results is determined.

C. Using centerline data and computer simulation more realistic estimates of error are possible.

D. When the complete two-dimensional data are obtained, eq (2) can be used for more realistic estimates of upper bound errors.

E. By using the complete data and the previously described computer program where integration is performed from the center to the outside, the actual level of truncation error can be determined for any direction in the far field.

3. Development of Sampling Criteria for Planar Near-Field Measurements on Spacecraft Antennas in an "Antenna Farm" Environment

In the actual near-field measurements, it is not practical to obtain continuous data as a function of the position vector $\underline{P}$; instead, data are obtained at equally spaced points of a rectangular lattice

$$\underline{P}_{r,s} = r\, \delta_x \underline{e}_x + s\, \delta_y \underline{e}_y. \tag{5}$$

The integral in eq (1) is also evaluated by a summation, and this combination of incremental data and summation has the potential for introducing an error, termed an aliasing error, in $D'(\underline{K})$. The magnitude and character of the error depends on the data point spacings δ_x, δ_y, and the spectral bandwidth of the measured data. In principle, if the spacings are made small enough the aliasing error can be reduced to the noise level; but if they are too small, both the measurements and calculations become inefficient. We desire techniques to predict the optimum data point spacings for a given application to achieve a given level of accuracy and methods to estimate the aliasing error. The details of these techniques will now be described.

We denote the actual measured data as $B_e(\underline{P})$ and the true spectrum of these measurements as $F(\underline{K})$. The term "true spectrum" as used here means that $F(\underline{K})$ is the Fourier transform of $B_e(\underline{P})$ and there are no aliasing errors in $F(\underline{K})$. The measured data include some errors due to such effects as scattering, nonlinearity, and noise, and these errors will have an influence on $F(\underline{K})$. We are therefore not excluding measurement errors and their effect on $F(\underline{K})$ at this point, only aliasing errors in the determination of the Fourier transform. In principle, this is accomplished by taking data at very close spacings, and conceptually $F(\underline{K})$ may be considered to have been calculated from data with δ_x and δ_y much less than $\lambda/2$, where λ is the operating wavelength.

If data are obtained at more realistic spacings, and the digital Fourier transform (DFT) used to evaluate the integral of eq (1), the result is

$$F_e(\underline{K}) = \sum_{m,n=-\infty}^{\infty} F(k_x + 2mk_1, k_y + 2nk_2), \tag{6}$$

where $k_1 = \dfrac{\pi}{\delta_x}$, $k_2 = \dfrac{\pi}{\delta_y}$.

The aliasing error is due to the contribution of the terms for $m \neq 0$, $n \neq 0$ within the region $|k_x| < k_1$, $|k_y| < k_2$. This is illustrated in figure 9 for a one-dimensional spectrum and shows how the sidelobes of the true spectrum overlap and cause errors in the calculated result. If the true spectrum is band limited, that is, if

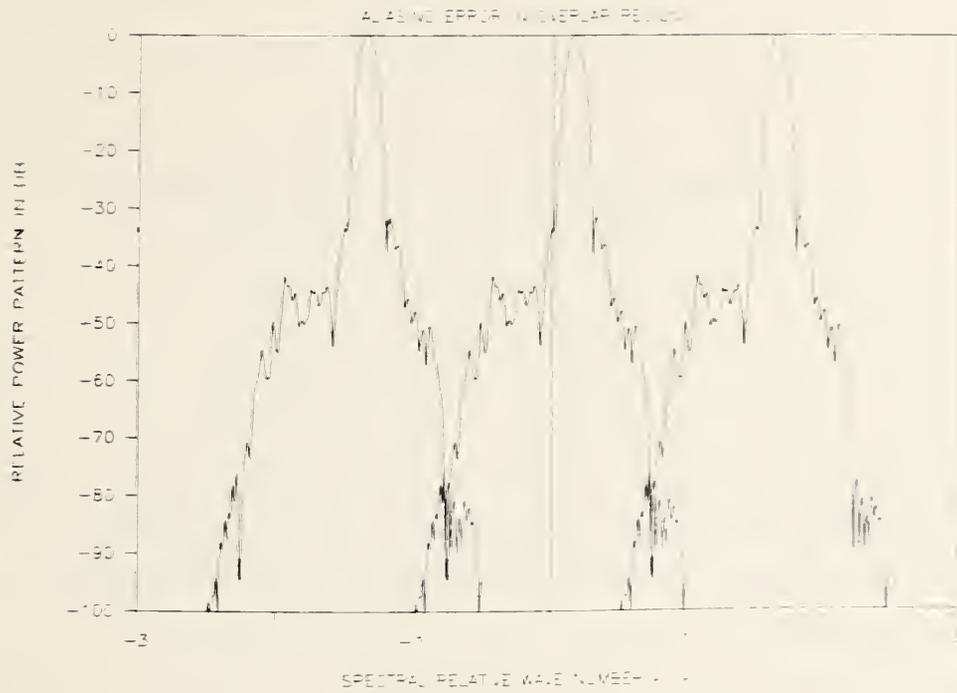$$|F(\underline{K})| = 0$$

14

Figure 9.   Aliasing error due to overlapping of offset spectra.

Figure 10.   Band-limited spectrum with no aliasing error.

for all values of $|k_x| > k_1$, $|k_y| > k_2$, as illustrated in figure 10, and the data point spacings are

$$\delta_x < \frac{\pi}{k_1}, \quad \delta_y < \frac{\pi}{k_2}, \tag{7}$$

then there is no aliasing error. This is because there are no contributions for the terms in eq (6) involving $m \neq 0$, $n \neq 0$ within the band-limited region. The problem of minimizing and estimating aliasing errors then reduces to determining the degree to which band limits k_1 and k_2 exist for a given antenna/probe combination. If a band limit does not exist, or if measurements are made at larger spacings than required by eq (7), we then need to estimate the magnitude and character of the resulting error spectrum produced by aliasing. This can be done from estimates of the test antenna and probe far-field patterns, from one-dimensional centerline tests, and from estimates or measurements of the random error in the measured data. Each of these will now be described in more detail.

The first case considered is the most conservative one where data point spacings of slightly less than $\lambda/2$ are used. An effective band limit is produced in this case from the exponential attenuation of evanescent waves, and random measurement errors are the source of the aliasing error spectrum. The true spectra as previously defined can be considered as composed of two parts,

$$F(\underline{K}) = D(\underline{K})e^{i\gamma d} + \varepsilon(\underline{K}), \tag{8}$$

the first term corresponding to the coupling product of probe and test antenna spectra, and the second arising from noise and other sources of error in the measured data. Since γ is defined by the relation,

$$\gamma = \sqrt{k^2 - (k_x^2 + k_y^2)}, \tag{9}$$

γ becomes purely imaginary when $k_x^2 + k_y^2 > k^2$, and the measured spectrum is exponentially attenuated by the factor $e^{i\gamma d}$ in eq (8). An effective band limit arbitrarily close to zero on the first term of eq (8) can therefore be obtained by choosing δ_x and δ_y so that

16

$$k_1 = \frac{\pi}{\delta_x} > k, \ k_2 = \frac{\pi}{\delta_y} > k. \tag{10}$$

The amount of attenuation or band limiting at the boundary of the k-space domain is

$$20 \ \log (e^{i\gamma d}) \cong -54.6 \ (\frac{d}{\lambda}) \ \sqrt{(K_B/k)^2 - 1} \ \ \text{dB} \tag{11}$$

where

$$K_B = \sqrt{k_x^2 + k_y^2} > \frac{\pi}{\delta_x} \ \text{or} \ \frac{\pi}{\delta_y}.$$

For instance, if $d = 3\lambda$, and $\delta_x = \delta_y = 0.4 \ \lambda$, $D(\underline{K}_B)$ is attenuated by at least 122 dB on the scan plane from its magnitude at the antenna surface. Since these evanescent modes are small for most antennas, there is an effective band limit for the first term in eq (8) if the data point spacing is slightly less than $\lambda/2$.

The second term in eq (8) arises from errors in the measured data; most of these are slowly varying at a function of x and y, and therefore also have band limits. It is generally the random errors, due to receiver noise, vibration of the probe, etc., which produce an error spectrum that does not have a practical band limit. It is this noise spectrum that generally sets a lower limit to the aliasing error effects. The magnitude of the noise level in the computed spectrum F($\underline{K}$) can be estimated from a knowledge of the random errors in amplitude and phase, along with certain other antenna and measurement parameters. A recent study [6] has shown that the ratio of the noise level in the spectrum to the peak value of the antenna spectrum is

$$\left| \frac{\epsilon(\underline{K})}{D(\underline{K}_0)} \right|^2 \leqslant \frac{18 \left(\sigma_\psi^2 + \sigma_a^2 (N/N_e) \right)}{N_e} \tag{12}$$

where

$\epsilon(\underline{K})$ = noise spectrum,

$D(\underline{K}_0)$ = peak value of antenna spectrum,

N = total number of measurement points,

N_e = number of points within the effective area of the test antenna,

σ_a = standard deviation of linear amplitude random error,

σ_ψ = standard deviation of random phase error in radians.

For typical measurements where $\sigma_a < 0.5$ percent, $\sigma_\psi < 0.5$ deg, the noise spectrum is on the order of 55 to 65 dB below the peak of the antenna pattern and will have little effect on either peak gain or moderate sidelobes of -30 to -40 dB.

To use eq (12), the standard deviations of the random amplitude and phase distributions are required. These can be obtained by measuring or estimating the contributions of such sources as resolution in analog-to-digital converters, receiver noise, scattering within the room, and random position errors. An alternate method makes use of near-field centerline data at spacings much less than $\lambda/2$ which allow calculation of the spectrum for values of either k_x/k or k_y/k beyond ± 1 as shown in figure 11. These data were taken at a z-distance of about 6 λ, and from eq (11) any actual evanescent modes are attenuated to such a low level they could not possibly be detected. The calculated spectrum in the evanescent region therefore represents the effect of errors in the measurement, and the relatively constant floor level in this region is a direct observation of the effect of random errors in the measured data. From this direct measure of the signal-to-noise ratio in the one-dimensional spectrum the corresponding signal-to-noise ratio for the two-dimensional data may be inferred. For instance, let the 1-D measurement be taken in the x-direction over a length ℓ_x' with the data point spacings δ_x'. The corresponding 2-D data will involve data point spacings δ_x, δ_y and scan lengths ℓ_x and ℓ_y. The noise level for the 2-D measurement will then be

$$\left| \frac{\varepsilon(\underline{K})}{D(\underline{K}_0)} \right|_{2-D} \simeq \left| \frac{\varepsilon(\underline{K})}{D(\underline{K}_0)} \right|_{1-D} \sqrt{\frac{\ell_x' \delta_y \delta_x}{\ell_x \ell_y \delta_x'}}. \tag{13}$$

The next case considered is one where pattern results for a narrow-beam antenna are required only over a limited region centered on or near $\underline{K} = \underline{0}$. The data point spacings may then be increased beyond the value specified by the sampling criteria, producing large aliasing errors outside the region of interest while limiting the errors within. For example, if the far-field region of interest is bounded by

$$\left| k_y \right| < k_{ym}, \quad \left| k_x \right| < k_{xm}, \tag{14}$$

only the evanescent spectra will alias into this region if

18

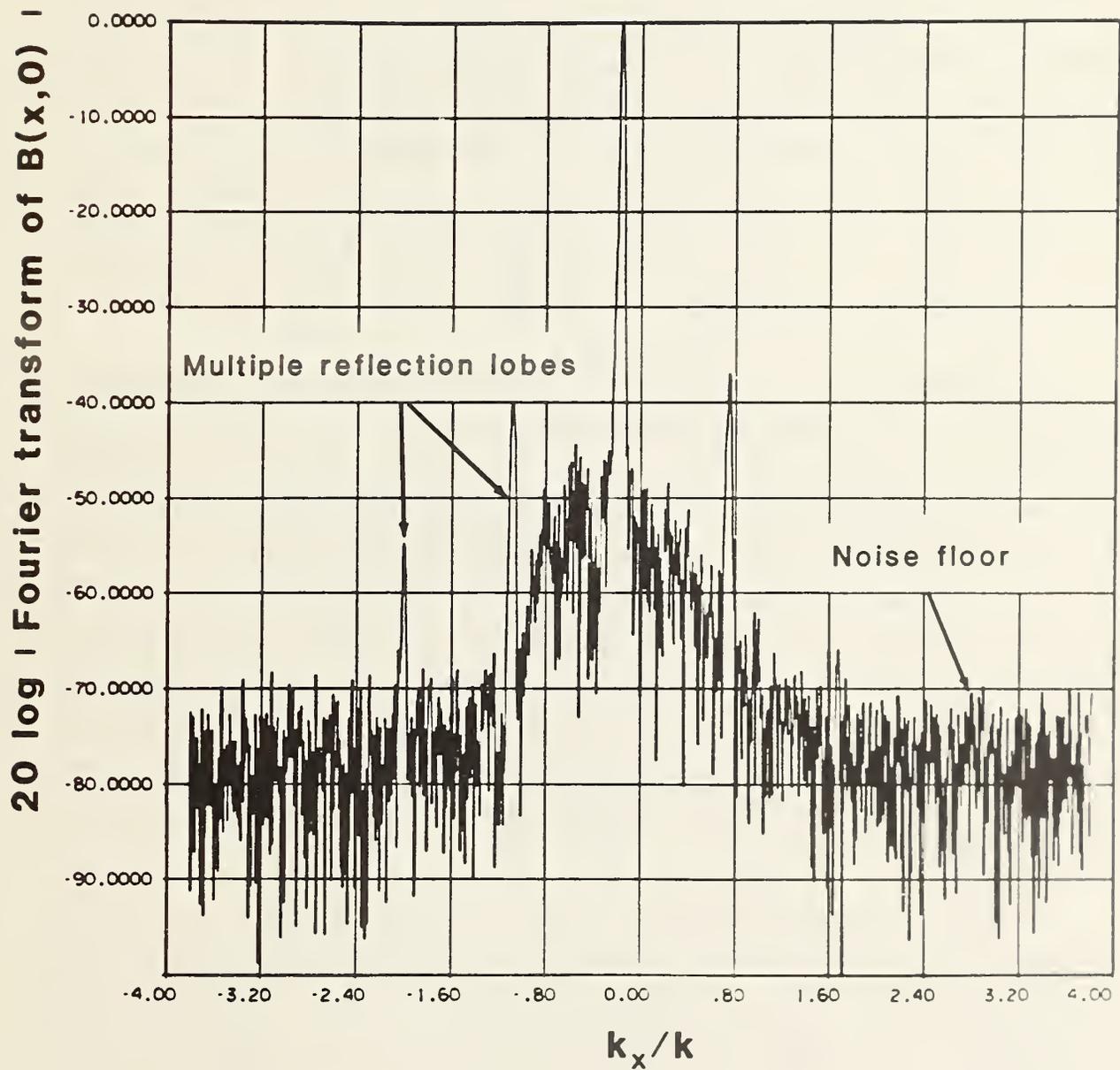Figure 11. Spectrum resulting from measurements at data spacings less than λ/2 showing noise spectrum in region where $k_x > k$.

$$\delta_x \lessgtr \frac{\lambda}{(1 + k_{xm}/k)}, \quad \delta_y \lessgtr \frac{\lambda}{(1 + k_{ym}/k)}, \tag{15}$$

as illustrated in figure 12. Measurement and data processing time can, therefore, be reduced by using the larger spacings with little change in accuracy within the region of interest.

The final situation is similar to the last one in that the data point spacing is larger than prescribed by the sampling criteria. In this instance, however, we are interested in estimating the errors in regions of the far-field where there is significant aliasing. One example of this situation is the region where $|k_y| > k_{ym}$ in figure 12, or all of the far field in figure 13 where a spacing of λ has been used. These situations generally arise where some accuracy can be sacrificed for measurement speed, but it is important to know how much error is incurred.

As before, this error is estimated from some knowledge of the antenna and probe patterns which together determine $D(\underline{K})$, and the data point spacing which determines the amount of overlap or aliasing. Either a graphical representation such as figures 12 and 13 or numerical values substituted into eq (6) can be used. The errors can also be estimated from centerline near-field measurements where initially spacings on the order of $\lambda/10$ are taken. The far field is calculated from these data representing the approximate antenna pattern. Similar far fields are then calculated using subsets of the data composed of every nth point. As the spacing increases, changes in far-field parameters such as gain, side-lobe level, etc. give a measure of aliasing errors. This technique is also very useful in determining or verifying the adequacy of a proposed spacing.

The analytical and measurement techniques described in the last two sections have been derived for arbitrary antennas and have been used successfully on a wide variety of types as shown previously in table 1. They should work just as well on the offset-reflector, shaped-beam antennas used on communications satellites.
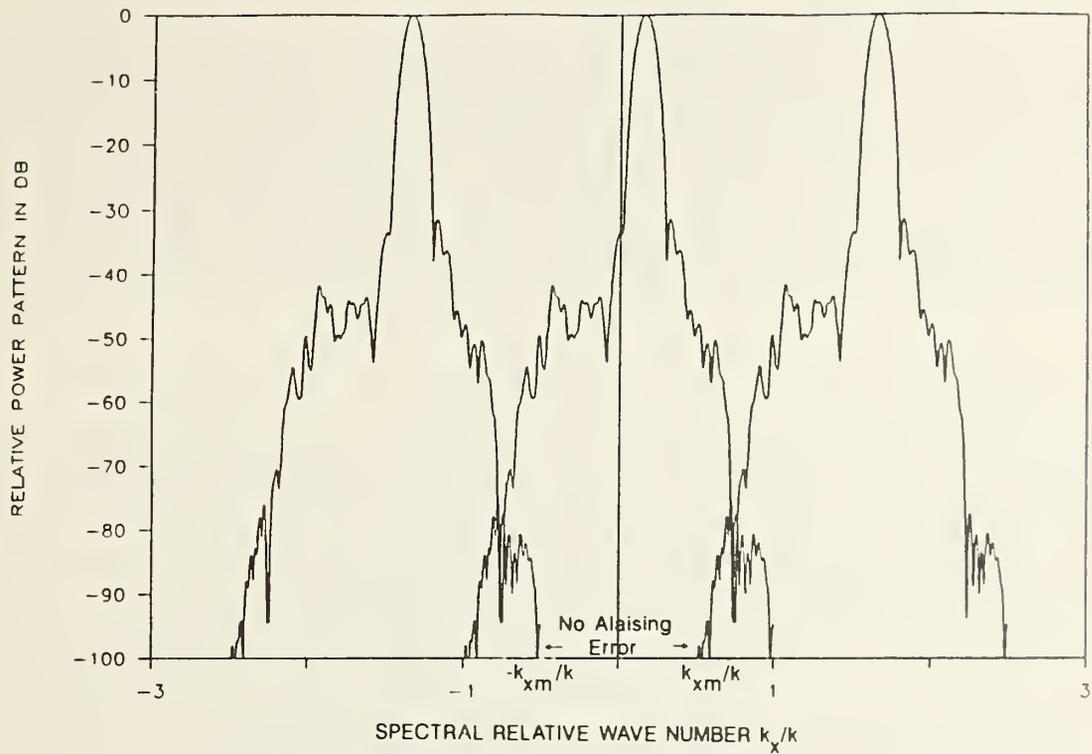
Figure 12. Data spacing greater than $\lambda/2$, with no aliasing error within the region $|k_x| < k_{ym}$.
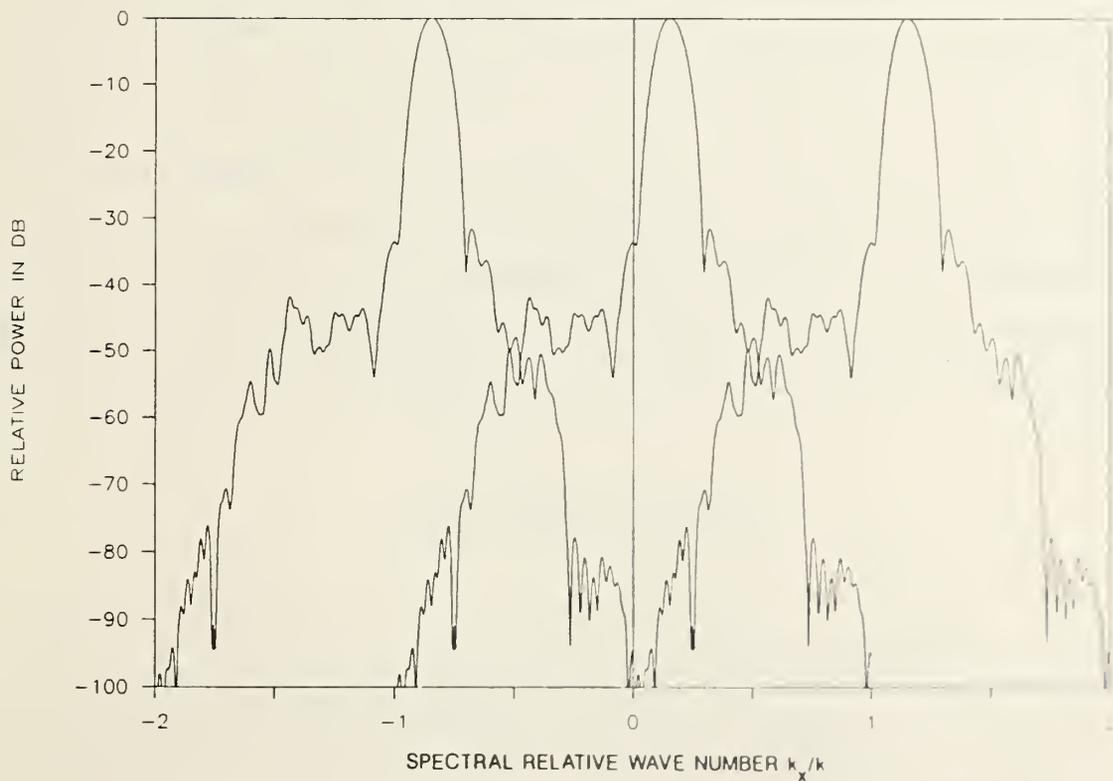
Figure 13. Overlapping spectra for data spacing of λ.

21

4. Development of Diagnostic and Design Assist Methods Which Make Use
    of Untransformed Near-Field Data

The intent of this approach is to try to reduce the time involved in both
the development and antenna performance verification test programs. The idea
is to compare the directly measured data with an expected or prescribed stan-
dard field distribution over the measurement plane, infer the reasons for dif-
ferences, and effect corrections, changes, or repairs in the antenna system.
We will now consider the various aspects of this approach.

4.1 Specification of a Standard Near-Field Pattern

It was not within the scope of this research to develop the capability
for calculating such standard near-field patterns, but this capability does
exist both within INTELSAT and with the various contractors working on the
antenna developments. From a specification of the feed array and the reflec-
tor position, shape, and orientation, the electric field on a plane coincident
with the measurement plane can be specified. This assumes of course that the
relative positions and orientations of the test antenna coordinates and the
measurement plane are known. The near-field system does not in general meas-
ure electric-field components, since the probe's directivity and polarization
will influence the measurement to some extent. For small probes with high
polarization purity, the near-field data is very nearly the same as the elec-
tric field. However, for larger probes the field is smoothed by the integrat-
ing effect of the probe aperture causing the near-field data to differ from
the actual field. It is not difficult to include the effect of the probe in
the calculation of the standard pattern however since its receiving spectrum
will in general be known. We will therefore assume that a standard pattern
which specifies the expected relative near-field data can be calculated and
denote it as

$$B_s(\underline{P}) = a_s(\underline{P})e^{i\psi}s(\underline{P}).$$

(16)

22

4.2 Comparison of Measured and Standard Data

The first point to keep in mind is that generally the complete near-field data over the full measurement area will be required before reliable comparisons can be made. Since the far field in each direction is determined from all the near-field data, complete near-field data will also be required for comparison. There may be some cases where single centerline data could identify major discrepancies, but if the differences are small, complete data are necessary.

The second point is that with the current state of development the comparison process will not be completely automatic. The interpretation of differences between measured and expected patterns will require a good deal of evaluation and judgement to determine the likely causes. For instance, a difference could be due to a translation in x, y, or z of the measurement plane relative to the chosen reference plane, and such possibilities should be explored before considering possible antenna problems.

One of the best methods for presenting the comparison data in a way that can identify even small differences and also present large amounts of data is a contour plot of phase difference or amplitude ratio. In most cases, the phase is the most sensitive indication of antenna problems. Some examples are identified below.

4.2.1 Beam Alignment

A phase difference which varies linearly with either x or y is an indication of the beam's being shifted in the far field. The amount of beam shift is given directly from the phase slope. If there is a linearly varying phase difference between the standard and measured patterns of $\Delta\psi$ over a distance Δ_y, then the beam will be shifted by the amount ΔE, where

$$\frac{\Delta\psi}{\Delta_y}\frac{\lambda}{360} = \frac{\Delta k_y}{k} = \sin(\Delta E). \tag{17}$$

4.2.2 Feed Alignment

If the feed is not at the focal point of the reflector, the near-field phase will show a quadratic character as shown in figure 14.

23
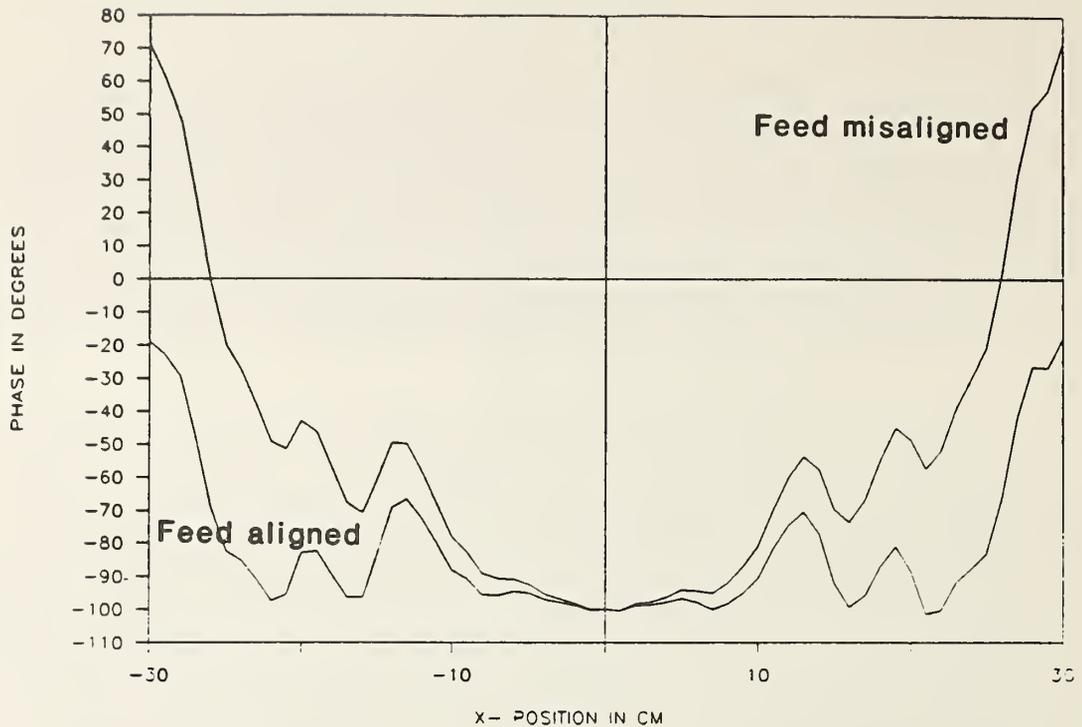
Figure 14. Quadratic phase error due to feed misalignment.

4.2.3 Reflector Surface Errors

If the feed is operating properly, the near-field phase data can identify
surface errors in the reflector. This was shown very graphically in measure-
ments on a compact-range reflector using a planar near-field scanner [7]. The
phase contours shown in figure 15 identify the location and magnitude of a
misadjusted support. When this support was properly aligned, the phase was
much more uniform as shown in figure 16. In this case, the phase was supposed
to be uniform across the reflector and so the measured phase was a direct
indication of departure from the desired. In more complex antennas such as
shaped-beam types, it will be necessary to compute the phase differences
before presenting the data.

4.3 Diagnostic Methods Involving Some Data Processing

In some cases, the feed may be the source of problems, and it would be
desirable to do some processing of the data to locate faulty elements in a
feed array. With this in mind, a more extensive study was initiated to

24
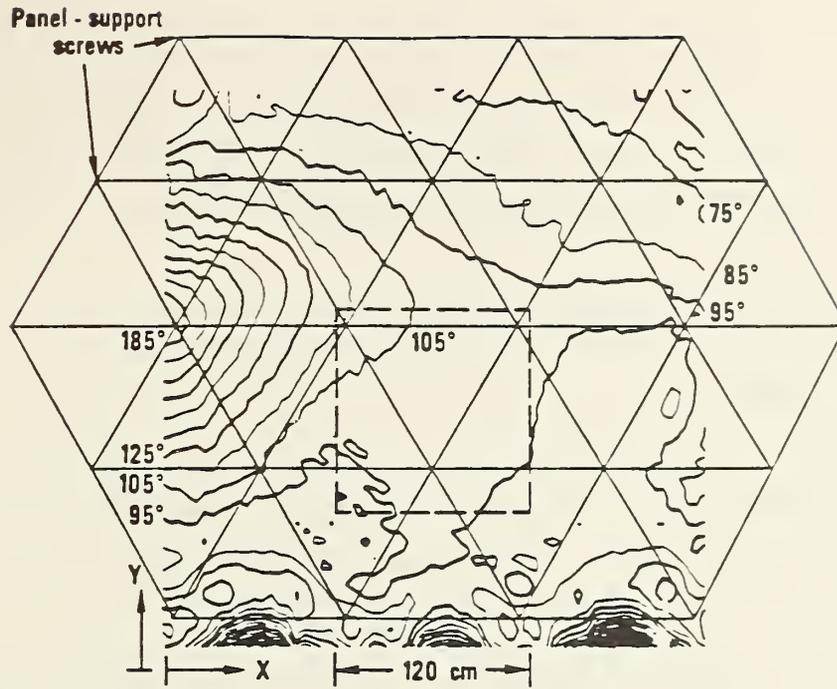
Figure 15. 10 deg phase contours for reflector with misaligned panels.
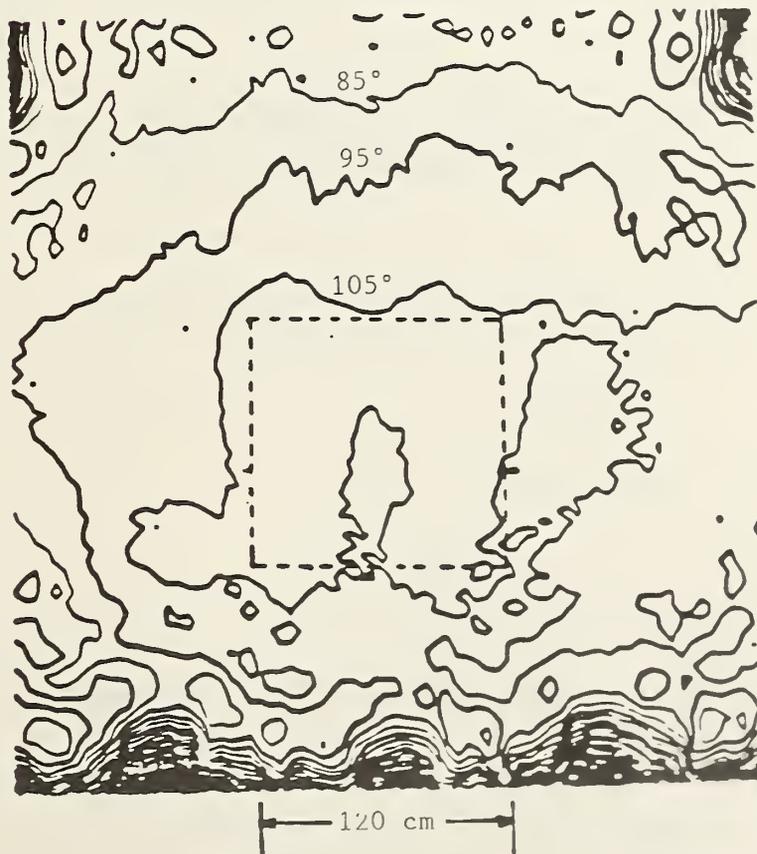
Figure 16 Phase contours after panels correctly aligned.

25

determine the utility of doing some processing of the near-field data to identify feed or reflector problems. This study compared the potential information obtained and the amount of data processing required with that already used in computing far-field patterns. This study involved a brief preliminary investigation into the following questions:

A. Given a desired far-field pattern, is it possible to predict probe output on a near-field measurement plane for subsequent comparison with measured near-field data?

B. For an antenna (or feed) with approximately planar aperture, is it possible to perform near-field measurements on a given plane and transform back toward the aperture to determine whether the aperture excitations are correct?

C. For an offset reflector antenna, is it possible to perform near-field measurements in front of the reflector and transform back toward the feed via the reflector to determine whether the aperture excitations are correct?

Discussion: A. Direct Near-Field Comparison. The electric field may be expressed everywhere in the forward hemisphere (z > 0) by the relationship [8],

$$\underline{E}(\underline{r}) = \frac{1}{2\pi} \int_{-\infty}^{\infty} \int \underline{b}(\underline{k}) \exp(i\underline{k}\cdot\underline{r}) \, d\underline{K},$$

$$d\underline{K} = dk_x dk_y,$$

$$\underline{K} = k_x \hat{x} + k_y \hat{y},$$

$$\gamma = k_z = \begin{cases} \sqrt{k^2 - K^2}, & k \geqslant K \\ i\sqrt{K^2 - k^2}, & k < K \end{cases}, \tag{18}$$

where $\underline{b}(\underline{k})$ is the plane-wave transmitting spectrum. Asymptotically, we also have:

$$\underline{E}(\underline{r})_{r\to\infty} \sim \underline{f}(\underline{r}) \exp(ikr)/(ikr), \tag{19}$$

where $\underline{f}$ is the far-field pattern.

Using the relationship,

$$\underline{f}(\underline{k}) = \gamma k \ \underline{b}(\underline{k}),$$ (20)

we may write E in terms of the far-field pattern:

$$\underline{E} = \frac{1}{2\pi} \int_{-\infty}^{\infty} \int \ \underline{f}(\hat{k}) \ \exp(i\underline{k}\cdot\underline{r}) \ \frac{dk}{\gamma k}.$$ (21)

In principle, eq (21) allows the determination of the field everywhere in the forward hemisphere, given the complex far-field. In practice, computed results are not valid in areas where evanescent (storage) modes dominate (the reactive zone). There is seldom any measurable error, however, as long as one avoids the region within several wavelengths of the aperture. The backward transform implied by eq (21) is a classic example of an ill-posed problem in which small errors, which arise in the measurement of the far field, result in exponentially large errors in the extreme near field. Even when the far-field pattern is supplied analytically, errors due to the truncation of the integration region and finite precision arithmetic eventually doom any numerical calculation of eq (21) as the aperture region is approached. However, using an exactly solvable model (a two-dimensional slit), Hamada and Yeh [9] have shown by example that the near field (beyond the reactive region) can be accurately reproduced numerically from the far field.

While the probe, of course, does not actually measure the electric field directly, the coupling between probe and AUT may be described in terms of the Kerns transmission formula,

$$b'(\underline{r}) = F \int_{-\infty}^{\infty} \int \ \underline{s}(\underline{k}) \cdot \underline{f}(\underline{k}) \ \exp(i\underline{k}\cdot\underline{r}) \ \frac{dk}{\gamma k},$$ (22)

where b' is the probe output, F is a known mismatch correction between probe and detector, and s is the probe's receiving pattern (which is simply related to the far-field pattern if the probe is reciprocal). Equation (22) is not numerically viable in the reactive zone, as discussed above. However, there is a more stringent limitation related to the assumption that multiple reflections between the probe and AUT may be ignored. In order to meet this condition, the probe and AUT must be separated by an experimentally determined distance, which usually places the probe well outside the reactive zone.

27

Equation (22) makes it possible to predict the output of a given probe on a near-field scan plane if the far field of the AUT is known. Efficient algorithms have been implemented to numerically evaluate the integral (basically a 2-D Fourier transform), and the computed output is produced on a rectangular grid on as fine a mesh as desired. Therefore, it is currently feasible, and possibly quite useful, to make real time comparisons between measured and predicted field distributions from the feed array. It should be noted, however, that the ultimate test is whether or not the far-field pattern meets specifications. Of course, the far-field pattern may also be obtained from the measured near-field data and the probe-receiving pattern, and with currently available capabilities, the necessary processing is inexpensive and requires only a few additional minutes on the computer. (The far-field pattern of an offset reflector may be accurately determined, using physical optics, from the far-field pattern of the feed array [see ref. 10].)

Using a direct near-field comparison, Repjar and Kremer [7] were able to adjust a millimeter-wave compact range reflector to obtain an acceptably uniform phase front. Hamada et al. [10] have used near-field data to fine tune an array feed for an offset reflector. Also, on at least one occasion, a standard near-field pattern measurement performed at NBS was used to pinpoint bad elements in an array which was known to have a pathological far field behavior [11].

Discussion: B. Transformation from Near Field to Aperture. As implied above, it is difficult to extract useful information on evanescent modes from a near-field measurement. While posing no difficulty if only the far field is to be computed, this is an obstacle if fields are required closer to the AUT, for evanescent waves become increasingly important as the aperture is approached.

It should be emphasized that far-field and near-field patterns theoretically contain the same information and that any technique which reconstructs an aperture field from the far field can be adapted for use with near-field data.

One approach in calculating approximate aperture fields is to simply perform the transformation (1), setting z = 0, and ignoring contributions from the nonpropagating part of the spectrum. While the result may not be totally

correct, it is certainly not devoid of information either and might be quite useful in gauging deficiencies in the feed-array excitation. Similar methods have actually been used to study surface irregularities in large dish antennas [12-14], where it has proven feasible to plot accurate surface contours using phase information from a projected aperture field.

Discussion: C. Transformation from Near Field to Aperture via Reflector. This point takes us beyond the plane-wave theory discussed so far in that it is no longer possible to relate the field near the feed to the field beyond the reflector with the simple transformation [10]. It might at first seem feasible to trace the rays in the measured spectrum back to the reflector, and then onto the feed region, but it is known that geometrical optics breaks down at caustics. An example of a caustic is the focal point of the reflector, the approximate location of the feed array.

An appropriate way to handle this problem uses the physical optics approximation, and procedures that can determine an appropriate feed excitation given a desired far field [15] have been devised. These procedures begin by bracketing the optimum pattern in an envelope of acceptability. The solution ultimately obtained is not a true inversion of the problem but is a likely candidate, being an aperture distribution which produces a far field which lies within the specified envelope and which may satisfy other constraints (e.g., on stored energy), as well.

Again, an aperture field constructed in this manner might provide useful diagnostic information.

Conclusions. We conclude that useful information is provided by any of the three methods A through C discussed above. A and B may be accomplished using software that already exists at NBS. C would require code that is probably best obtained from other sources. Each of the three approaches provides roughly the same information content, though in different forms. While the practical utility of A and B has been demonstrated in certain instances, ultimately, the determination of the best attack in a given situation depends on an experimental, and subjective, evaluation.

5. Development of Beam Alignment Techniques

5.1 Introduction

One result of any antenna measurement, whether it involves far-field, anechoic chamber, compact range, or near-field techniques, is a far-field pattern such as figure 17. In these patterns, the transmitted or received power is specified as a function of angle, and these angles are defined with respect to a measurement coordinate system. In far-field, compact range, or anechoic chamber measurements where the antenna under test is mounted on a two-axis rotator, the measurement coordinate system is fixed to and defined by the rotator as shown in figure 18. The angles in plots such as figure 17 are obtained directly from the angle encoders on the two-axis rotator. It is implicitly assumed that the two axes of rotation are mechanically aligned orthogonal to each other, and they therefore represent the theta and phi angles of a spherical coordinate system. In evaluating beam pointing accuracy, any mechanical misalignment of the rotator or errors in the encoders will produce corresponding errors in the measured angles.

The precise definition of the measurement coordinate system is only one part of the requirements for accurate beam-alignment determination. Since the AUT will in most cases be removed from the measurement system for actual use, we need to know how these measured angles are defined in the antenna coordinate system. In the case of the rotator this would involve the relative orientation and displacement of the AUT and the rotator coordinates.

In general, for any system the steps required in antenna boresight or beam alignment measurements are as follows:

A. Define the measurement coordinate system, denoted C_m, and the techniques used to prescribe its location and/or orientation.

B. Define the methods for measuring directions relative to the measurement system and the estimates of uncertainty caused by the various sources of error.

C. Define the AUT coordinate system, denoted C_a, and the methods used to prescribe it in a known, fixed location on the antenna.
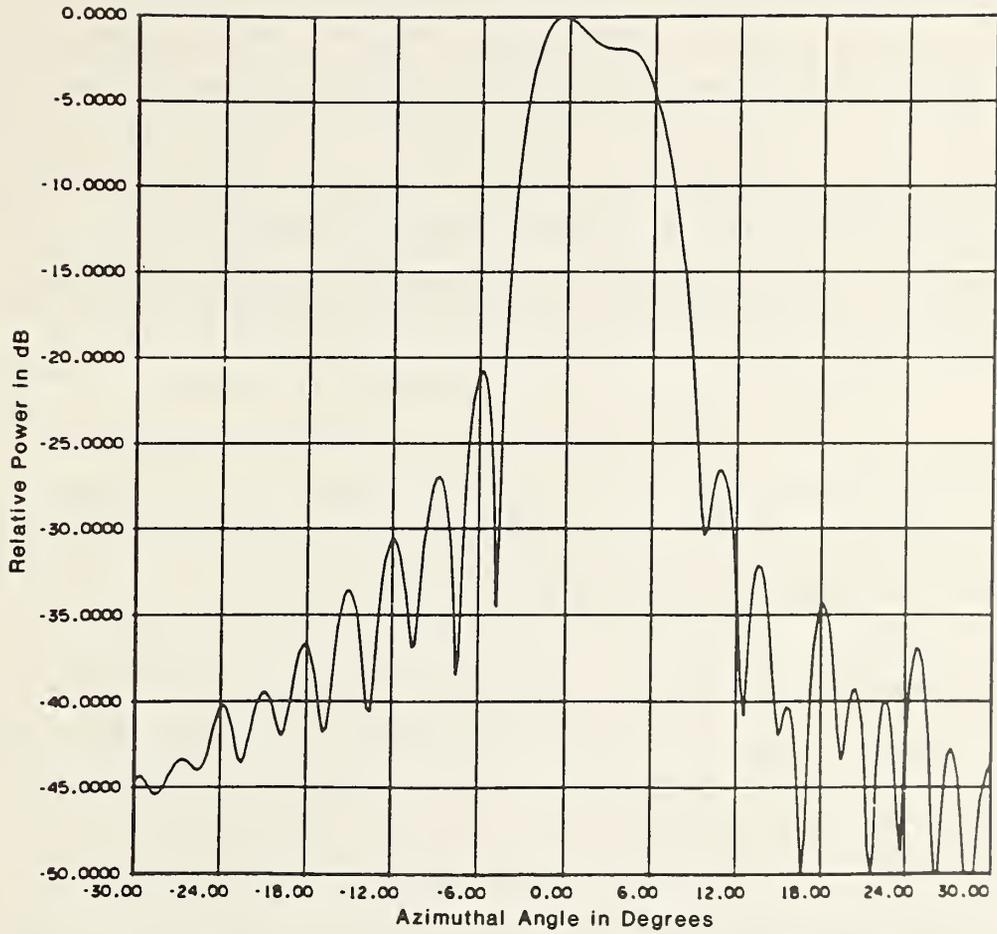
30

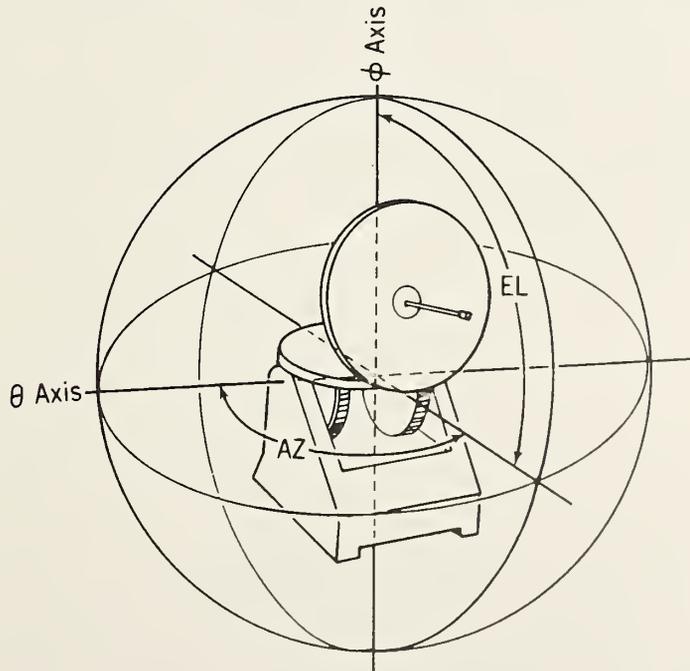Figure 17. Sample far-field pattern from antenna measurements.

Figure 18. Schematic of far-field rotator showing measurement and antenna coordinates.

31

D. Prescribe methods for aligning the AUT such that there is a known re-
    lationship between C_m and C_a, and determine the relationship between
    directions measured in C_m and corresponding directions with respect
    to C_a.

E. Determine the uncertainties in step 4, combine them with those in
    step 2, and obtain an estimate of total uncertainty.

F. Perform alignments and measurements to demonstrate the validity of
    estimated errors.

Each of these steps will now be described in detail as it applies to a planar
near-field measurement system. Even for this specific system, there are a
number of ways by which these steps could be implemented, and we will describe
the approach used at NBS as one example.

5.2 Alignment Adjustments

The alignment process makes use of a variety of instruments for measuring
position, displacement, and angular rotation, and since these will be referred
to throughout this discussion they will each be described.

5.2.1 Theodolite Autocollimator

One of the most useful alignment instruments is a precision theodolite
with the additional features of an optical autocollimator and optical microm-
eter. The basic theodolite consists of a high-power telescope and precision
scales to measure azimuth and elevation angles defining the orientation of the
telescope in the theodolite coordinate system. The zero for the azimuthal
angles can be set at any arbitrary direction, but the elevation angles are
measured with respect to vertical using an internal electronic level. Both
angular scales have a resolution of 1 arc second and an estimated uncertainty
of ±2 arc seconds. The autocollimation feature is used extensively and con-
sists of a small, internal light source which projects an image of the cross-
hairs to a mirror located along the telescope's line of sight. If the mirror
is perpendicular to the optical axis, the projected crosshairs will be
reflected by the mirror and appear superimposed on the original crosshairs.
In this way, the optical axis of the transit can be transferred to the optical
normal of the mirror. If the front and back surfaces of the mirror are

32

parallel, the axis is further transferred to the mechanical mounting surface. If the mirror is mounted in a rigid fixture in a permanent location in the laboratory, it will permanently retain a definition of a particular axis which can be reestablished after the theodolite has been removed. For instance, in the alignment of the planar scanner a mirror is permanently mounted behind the scanner and adjusted so that its surface is parallel to the x-y measurement plane. In subsequent antenna alignments the autocollimator is aligned to the mirror and then used to align the antenna to that same reference. Under normal operating conditions the uncertainty in the collimation of the transit to the mirror is ±5 arc seconds.

5.2.2 Optical Micrometer

The optical micrometer is attached to the objective end of the telescope and utilizes prisms to produce an apparent translation of the crosshairs relative to the target without actually moving the theodolite. The amount of translation can be measured to within ±0.002 cm.

5.2.3 Laser Interferometer

A laser interferometer is used in many ways both in the operation of the scanner and in the alignment and definition of the scan plane. The interferometer is capable of measuring relative changes in displacement either along or normal to the axis of the laser beam. To accomplish this the laser produces two orthogonally polarized beams at frequencies f_1 and f_2. The electronics compares the frequency difference before they are radiated and after the two beams have been directed along separate paths and reflected back to the detector. Any difference in the Doppler shift of the two beams due to relative movement of any of the optical components is converted to a corresponding position change and displayed by the electronics. For instance, in the displacement mode where the position is measured along the axis of the laser beam, the optical arrangement is shown in figure 19. The reference beam at frequency f_2 is reflected back to the detector by the reference interferometer while the measurement beam at f_1 continues on to the cube corner reflector where it is also reflected back to the detector. Any relative movement along the axis of the beam between the reference interferometer and the cube corner reflector will produce a change in the frequency difference and be
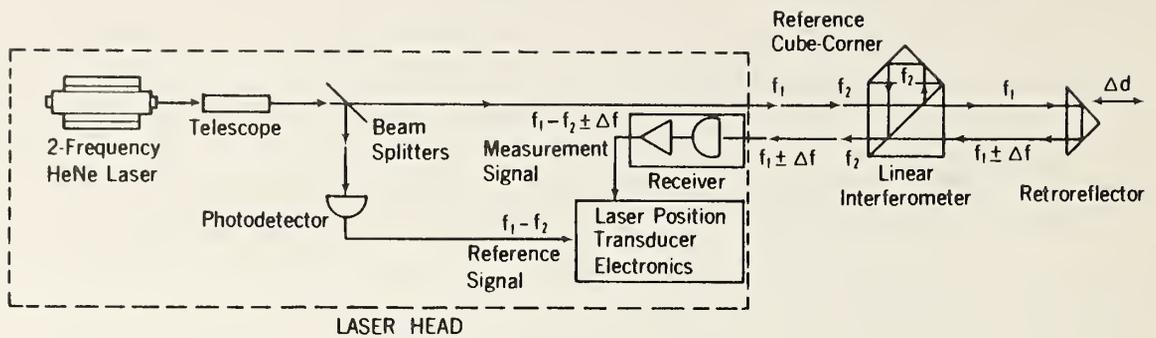
Figure 19. Schematic of laser interferometer distance measurement system.

interpreted as a relative position change. However, identical movement of both optical pieces along the beam, their translation normal to the beam, or rotation of the optics will have no effect on the position reading.

In the straightness mode different optics are used as shown in figure 20. In this case the straightness interferometer separates the two beams by equal and opposite angles θ_d. The straightness reflector is composed of two flat mirrors which are also rotated from a plane by the same angle θ_d, and therefore reflect the two beams back to the interferometer and then to the detector. Movement of either the interferometer or the reflector normal to the beam and in the plane defined by the two diverging beams will produce a relative Doppler shift and corresponding change in measured displacement. If the mirrors are flat, motion of either optical component along the beam or normal to the plane of the two beams will produce no position change. The reference line or "straight-edge" for the straightness measurements is not the laser beam, but the direction defined by the bisector of the angle between the two mirrors. This means that the straightness reflector should not move during the measurement since we cannot distinguish between transverse motion and rotation of the reflector. It also means that if displacement is to be measured relative to a specific axis, such as a horizontal or vertical line, the bisector of the straightness reflector must be aligned along that precise direction. Conversely, if straightness is measured for some arbitrary orientation of the reflector and we then need to define or transfer that direction

34

f_1 f_2 f_1 f_2 $f_1 \pm \Delta f_1$

2-Frequency HeNe Laser Telescope Beam Splitters

$f_1 - f_2 \pm \Delta f$ Measurement Signal

$F_1 \pm \Delta f_1$
$f_2 \pm \Delta f_2$

Receiver

$f_1 \pm \Delta f_1$
$f_2 \pm \Delta f_2$

θ_d

$f_1 \pm \Delta f_1$
$f_2 \pm \Delta f_2$

Δd

Photodetector

$f_1 - f_2$ Reference Signal

Laser Position Transducer Electronics

Straightness Interferometer

LASER HEAD

Figure 20. Schematic of laser interferometer straightness measurement system.

to a mirror or to the theodolite an auxiliary device must be used. Generally, that auxiliary device is the optical autocollimator. By collimating alternately on the two mirrors in the straightness reflector, as illustrated in figure 21, the location of the bisector can be determined and defined by a particular set of theodolite angles. That bisector or straight-edge reference line can then be rotated into any desired location, or the direction of the theodolite axis transferred to a permanent reference such as a reference mirror. If the autocollimator has to be located more than 2 to 3 m away from the straightness reflector in the above process, the small size of the mirror produces a very faint image and makes collimation difficult. This difficulty can be overcome by a two-step process that transfers the location of the bisector to a larger flat mirror placed on the front of the straightness reflector mount as shown in figure 22. The theodolite is placed close to the straightness reflector, and rotated to place its optical axis coincident with the bisector axis as previously described. A flat mirror is then placed on the front of the reflector mount as shown in figure 22, the theodolite is collimated on the mirror, and the change in transit angles noted. In future use where the transit is located farther away from the reflector, the larger mirror is used to provide a better image for collimation, and the reflector is rotated by the measured offset angles to place the straight-edge reference line parallel to the transit axis.
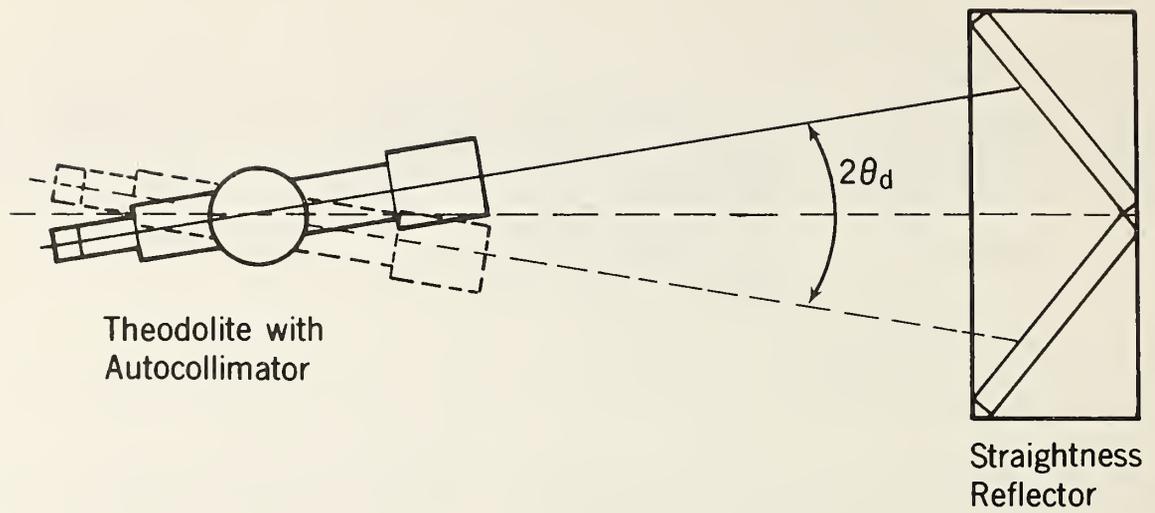
Figure 21.   Method for locating straightness reference line on
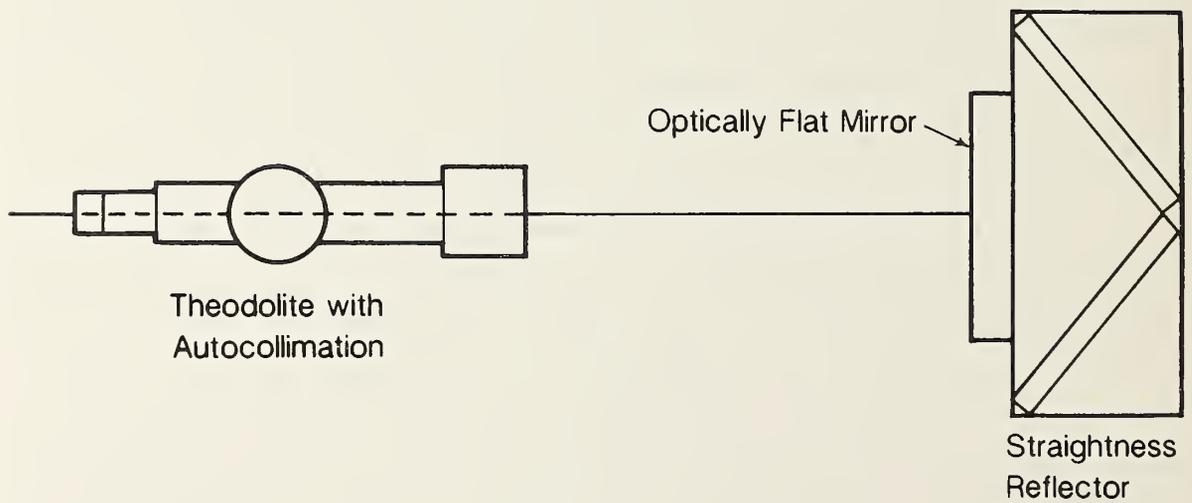straightness reflector.

Figure 22.   Method for transferring straightness reference direction to
flat mirror on surface of mirror mount.

5.2.4 Electronic Level

The fourth instrument used extensively in the alignment process is an electronic level or tilt meter which measures angular rotations with respect to a vertical axis. It has a resolution of 1 arc second and can measure changes in rotation as a function of position or determine the deviation of a surface from a horizontal or vertical plane.

5.2.5 Optical Square

In cases where it is necessary to obtain a precise 90 deg rotation in an optical axis an optical square is used. It is composed of two mirrors mounted in a fixure with a 45 deg angle between them. An incoming beam is rotated by 90 deg regardless of the orientation of the fixture to the incoming beam.

These five instruments, along with the laser sources, optically flat and parallel target mirrors, and other auxilliary mounting and adjustment devices are used in a variety of combinations to carry out the alignments and measurements necessary for antenna boresight measurements.

5.3 Definition of the Measurement Coordinate System, C_m

In planar near-field measurements, the x-y plane of C_m is defined by the "best fit" plane of the mechanical scanner. We want to determine the orientation of that plane in the laboratory and place a target mirror in a convenient location with its surface parallel to the measurement plane. The target mirror can then be used in future alignment of antennas.

In the box-frame design of the mechanical scanner shown in figure 23, the top and bottom horizontal rails along with the two vertical rails on the movable tower are the guides for the probes and therefore define the measurement plane. We will assume that these rails have previously been aligned to provide almost planar motion of the probe and that this plane is close to a vertical plane. The details of this alignment will not be described here since the current task is to locate and define the measurement plane once the scanner has been aligned.

In principle, the scan plane can be defined by using either a dual theodolite system or a single theodolite and the optical micrometer. In the dual theodolite system, the two theodolites are located at opposite ends of the
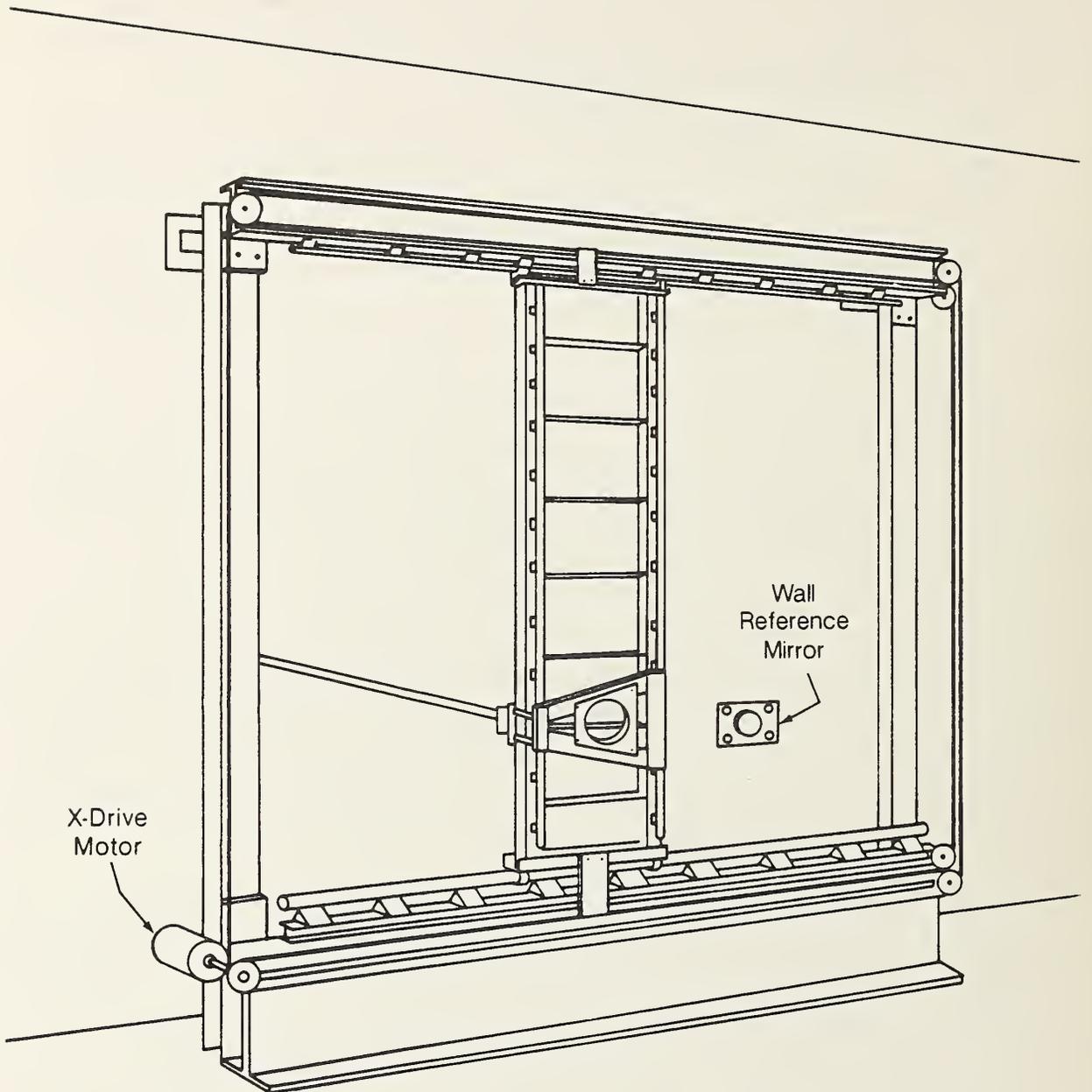
Figure 23. Schematic of box frame near-field scanner.

38

horizontal axis, approximately centered in the vertical direction, and collimated on each other. Azimuth and elevation readings are taken with each theodolite focused on a tooling ball placed at the probe location. Readings are repeated at each (x,y) position and are then converted to $\Delta z(x,y)$. In a similar way, an optical micrometer is attached to a single theodolite and direct readings of $\Delta z(x,y)$ are recorded. In both of these procedures, the setting of the probe and reading of the theodolites are manual and require long measurement times. As the probe is moved away from the theodolites the accuracy of setting decreases. Most of these problems are overcome by using the laser interferometer and electronic level to perform and digitally record the measurements.

The laser measurements begin by mounting the reference mirror shown in figure 23 on a very stable support behind the scan plane, and initially aligning it to the leveled autocollimator so that its surface is vertical and approximately parallel to the scan plane. The laser interferometer with the straightness optics is configured to measure the z-deviation of the bottom rail as a function of scanner x-position as shown in figure 24. This deviation is denoted $\Delta z_B'(x_S)$, where x_S denotes the scanner's x-reading. The straightness reflector is then rotated about its vertical axis, thereby rotating the straightness reference line until there is no linear variation in the z-deviation and this final data is denoted $\Delta z_B(x_S)$. A sample set of data is shown in figure 25. The straightness reference line is now parallel to the best-fit line of the bottom rail, and the next step is to transfer the orientation of this line to the reference mirror. The theodolite is first collimated through the optical square to the direction of the straightness reference line and then the reference mirror is readjusted for collimation in the azimuthal direction as shown in figure 26. The mirror's elevation adjustment is kept constant, and the plane of the mirror is now parallel to a surface defined by the best-fit line of the bottom rail and a vertical line. This plane is not necessarily parallel to the scan plane since the top horizontal rail and the vertical rails also affect the probe motion, but it serves as an intermediate reference plane.
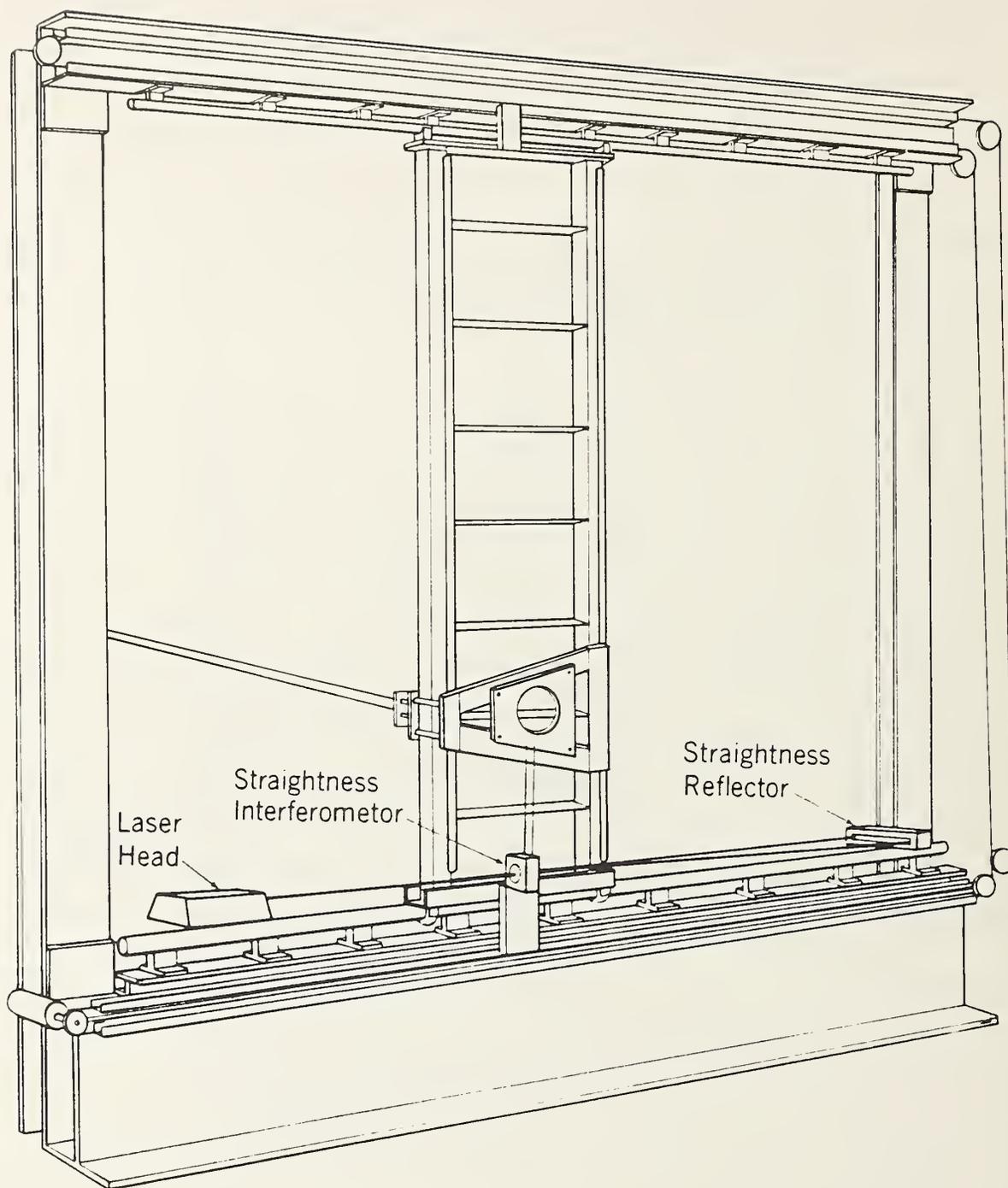
Figure 24. Straightness interferometer used in measurement of bottom rail of planar scanner.
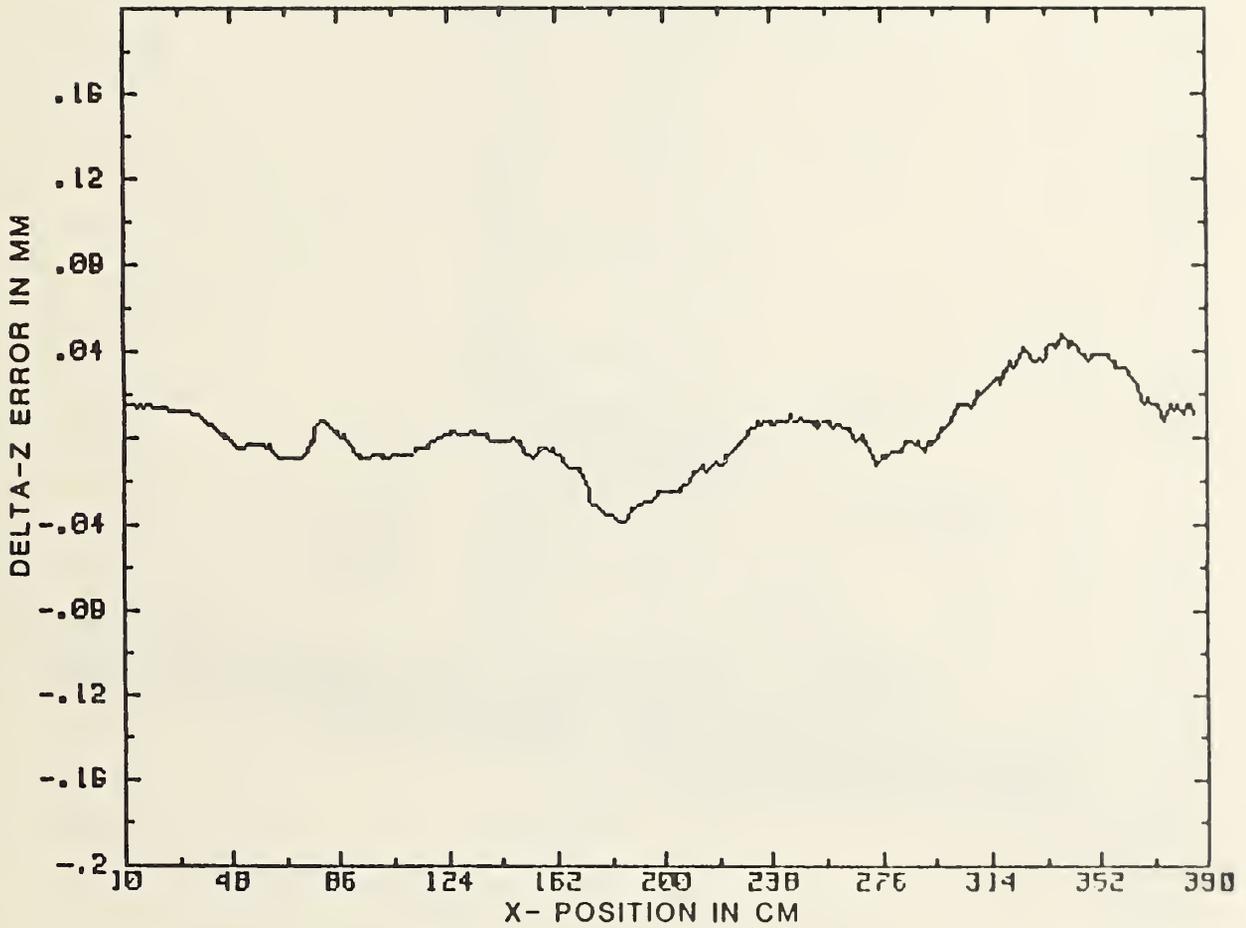
Figure 25. Deviation of bottom rail of scanner from straightness reference line.

41

Reference
Mirror

Optical
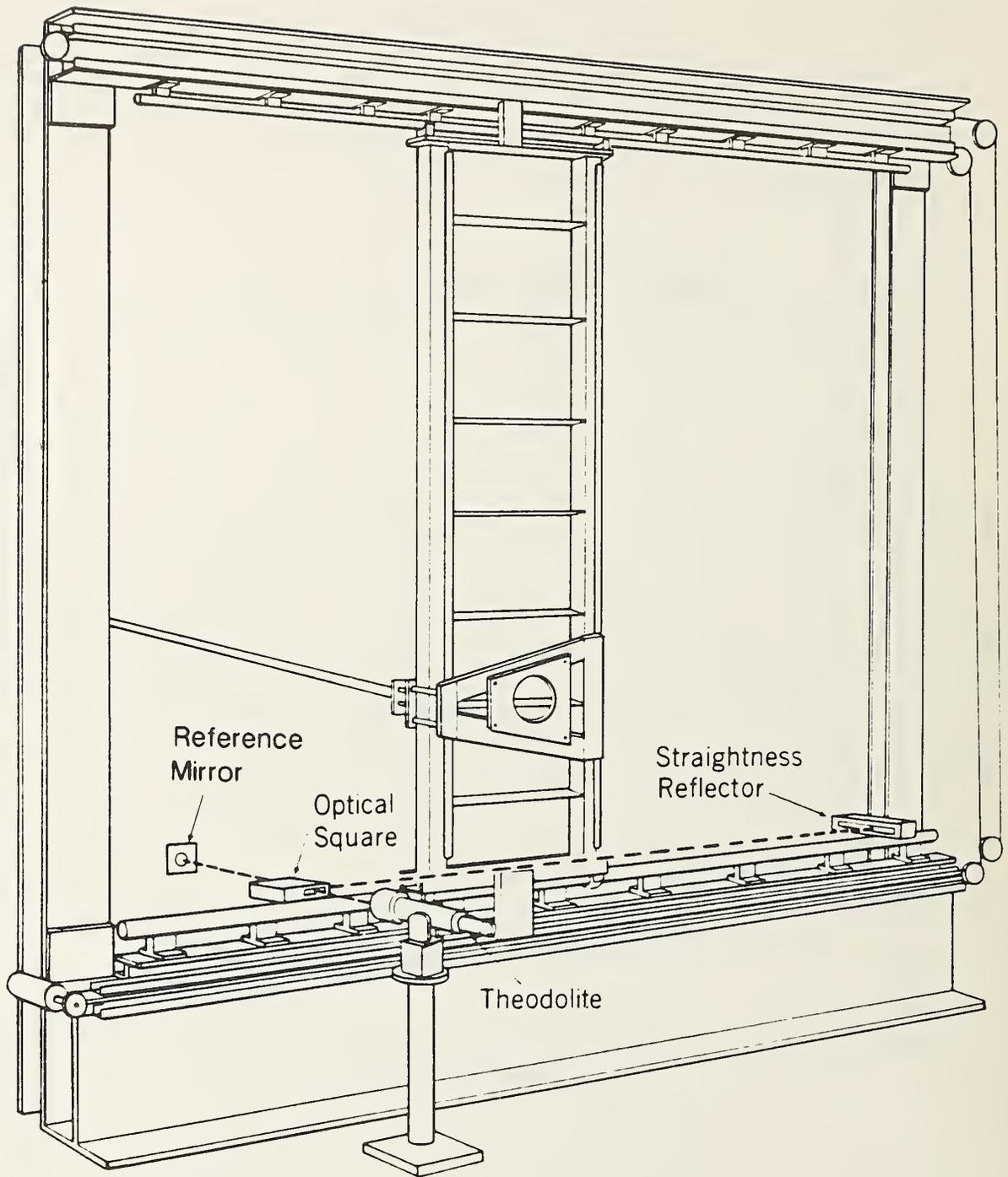Square

Straightness
Reflector

Theodolite

Figure 26. Theodolite and optical square arrangement used in transferring
straightness reference line to measurement system reference
mirror.

42

The vertical tower of the scanner is next placed in the position where $x_s = 0$. Using the theodolite with its axis horizontal, and the optical square to redirect that axis vertically, the reference line of the straightness reflector is oriented vertically. The straightness interferometer is then moved in the y-direction by the probe carriage and the z-deviation, $\Delta z_t'(0,y_s)$ is measured as a function of the scanner y-position, y_s. A sample set of data is shown in figure 27.

In principle, the measurement of $\Delta z_t'$ with the laser could be repeated at a sequence of x-positions; however, the vertical alignment of the straightness reflector at each x-position is time consuming. If the vertical tower is rigid, the rails will have the same relative straightness at each x-position and only the tilt of the tower about the x-axis will produce a change in z. This tilt change can be measured quickly and accurately with the electronic level as shown in figure 28. The tilt meter is set to zero at $x_s = 0$, and at closely spaced x-positions, $\theta_x(x_s)$ is recorded.
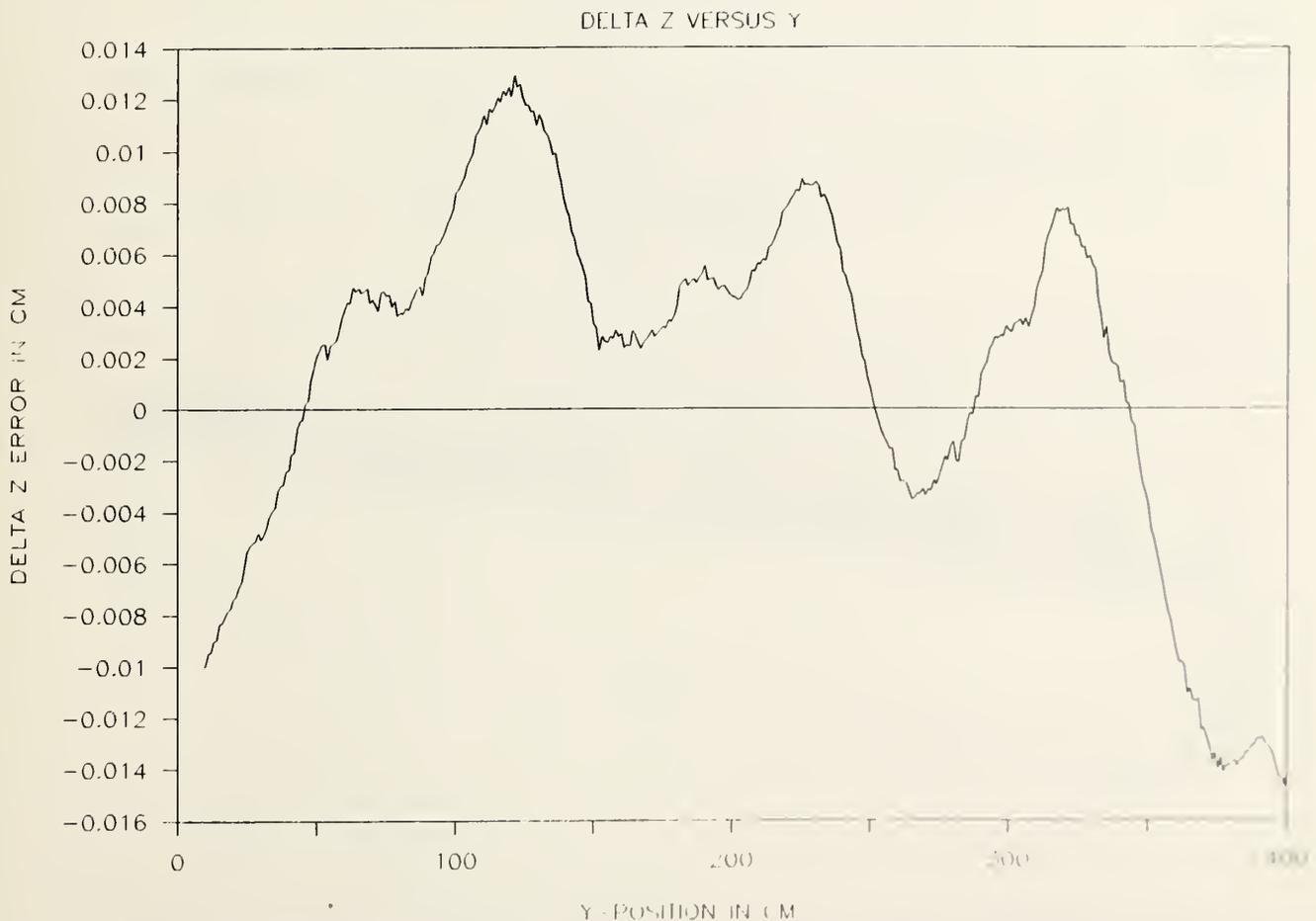

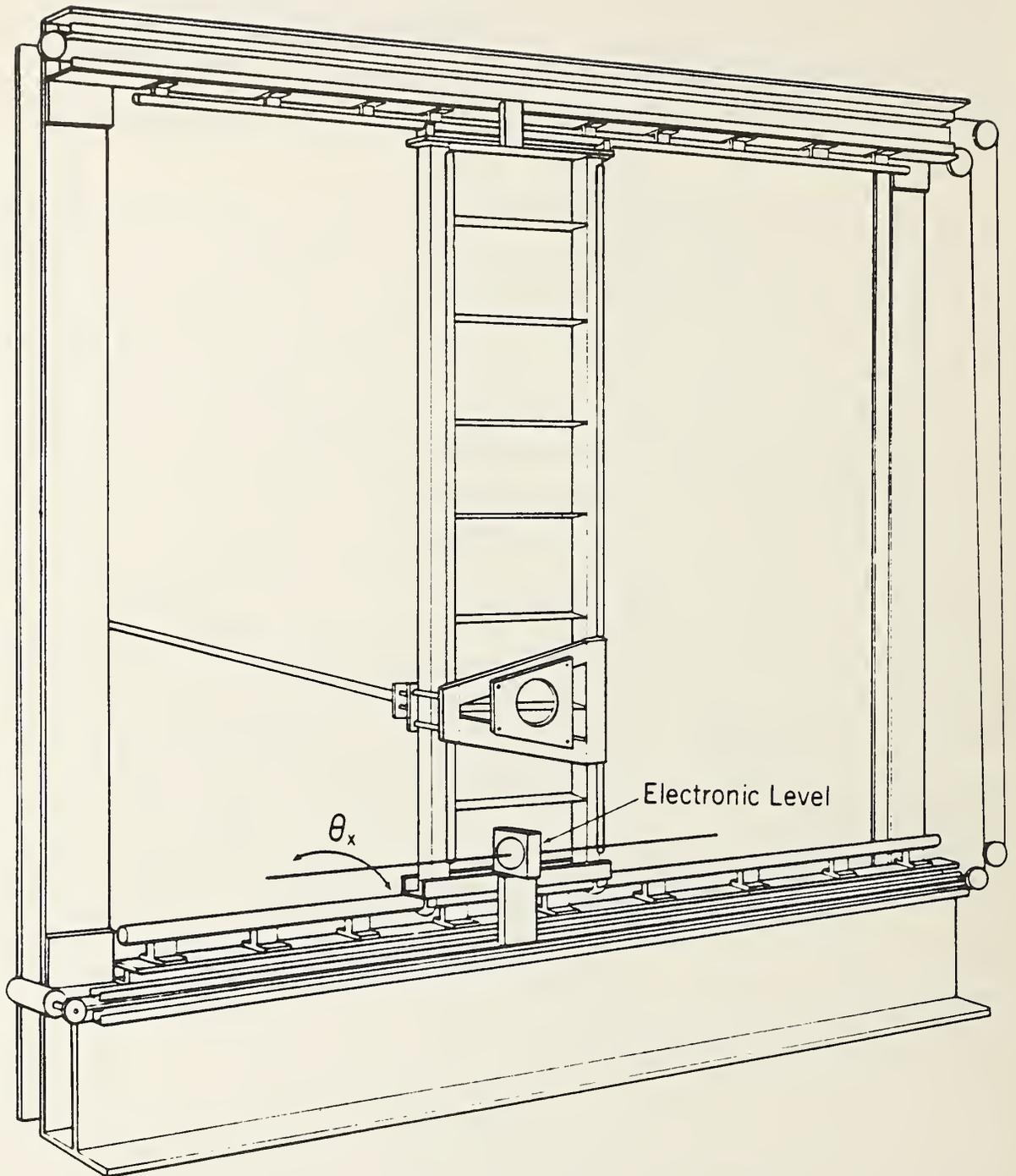Figure 27. Deviation of vertical rails from vertical reference line.

43

Figure 28.   Schematic of tilt meter on scanner to measure rotation of tower about the horizontal x-axis.

44

These three measurements are finally combined to give $\Delta z'(x,y)$ over the complete measurement plane using the relation

$$\Delta z'(x,y) = \Delta z'_B(x_s) + \Delta z'_t(0,y_s) + y_s \sin(\theta_x(x_s)). \qquad (23)$$

The primes indicate that these data are measured with respect to a vertical reference plane. Fitting these values of $z'(x,y)$ to a linear equation in x and y will give the plane that best fits the data and indicates the rotation of that plane in azimuth and elevation to the plane defined by the current orientation of the reference mirror. Once these rotations have been determined the reference mirror can be rotated, placing it parallel to the best-fit plane.

In using eq (23) to calculate the z-error, rotations of the tower and the probe transport about their y-axes have been neglected. Since the z-error produced by the y-axis rotations are proportional to the cosine of the rotation, and the angles are small, this is a good approximation.

The estimates of uncertainty in the angular location of the z-axis of the measurement plane are summarized in table 2. In combining each of the individual errors, we assume that they are independent, uncorrelated, and the estimated errors are upper bounds.

Table 2. Estimate of error in defining scan plane using straightness laser.

| Source of error	Estimate of error (arc seconds) in azimuth or elevation
Reference mirror alignment to straightness reference line	
Definition of straightness line	10
Optical square error	2
Collimation error	
To straightness reflector	5
To reference mirror	5
Mathematical fitting error	6
Final alignment of mirror to best-fit plane	5
Reference mirror stability	3
Root Sum Square	15
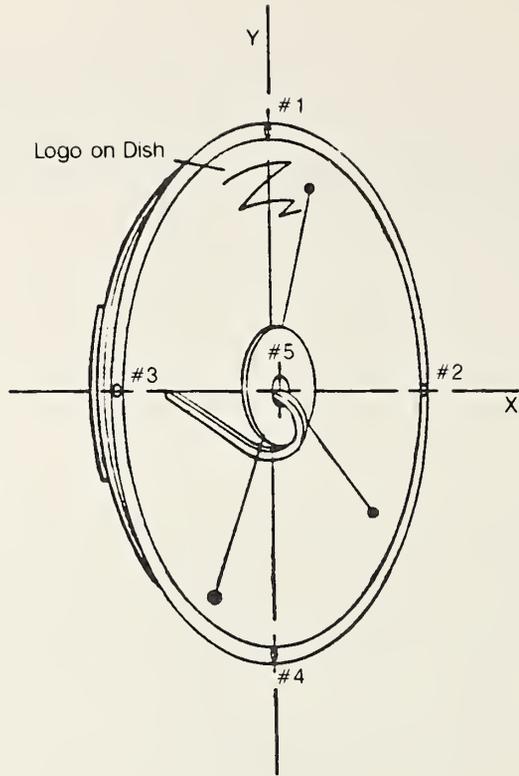
Figure 29. Antenna with fiducial marks to define x- and y-axes.
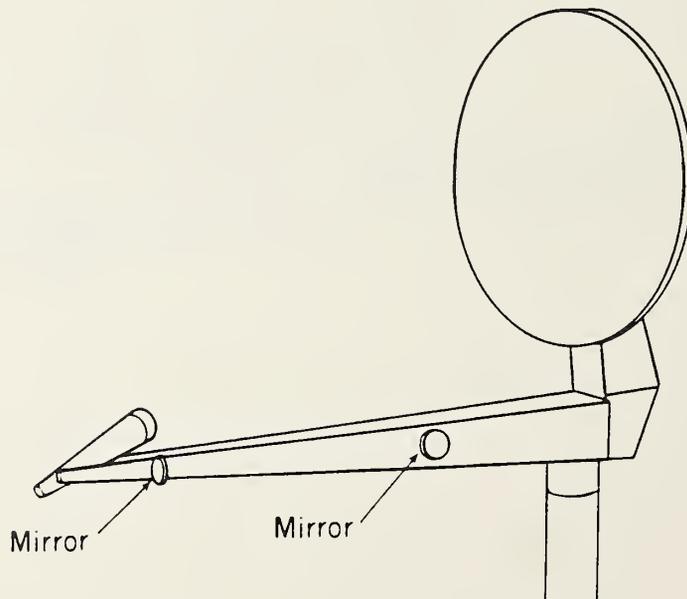

Figure 30. Mirrors on antenna to define its coordinate system.

46

5.4 Defining Antenna Coordinates

There are a number of possible ways to define the antenna coordinates,
and each will require different methods for aligning to the measurement sys-
tem. The most frequently encountered will be described. In one method shown
in figure 29, fiducial marks define the x- and y-axes and three points on the
surface define the x-y plane. Another method is illustrated in figure 30
where mirrors attached to the antenna define the x- and z-axes. By defini-
tion, the y-axis is then orthogonal to both of these. The translational loca-
tion of the axes can be identified with fiducial marks or, if the transla-
tional location is not critical, it can be arbitrarily defined during the
measurement by the (x,y) zero setting of the laser. Finally, a method
frequently used on far-field ranges is to specify the location of the z-axis
with a boresight scope attached to the antenna or its mounting bracket. The
angular location of the x- or y-axis can then be fixed with an orthogonal
mirror, a level attached to the antenna, or by fiducial marks.

5.5 Aligning the Antenna Under Test (AUT) to the Measurement Coordinates

If the antenna coordinates are defined by fiducial marks and three points
on the surface, the alignment is accomplished using mechanical means as illus-
trated in figure 31. The micrometer is fitted temporarily to the end of the
probe and brought sequentially into contact with the three reference surfaces.
The antenna is then rotated about its x- and y-axes until the micrometer read-
ing (corrected for the Δz error) at each of those points is the same. The
antenna is then rotated about its z-axis until its x-axis is parallel to the
x-axis of the scanner.

If the antenna axes are defined by mirrors or by the boresight scope, the
theodolite autocollimator is used and the antenna is rotated until the optical
axis is parallel to the reference mirror which defines the measurement system
z-axis. Since the reference mirror is fixed in a certain location, and the
AUT is generally at a different height, we must effectively transfer the
reference mirror to a new location. This can be done by using two theodo-
lites, one positioned to collimate on the reference mirror and one positioned
to collimate on the antenna. As shown in figure 32 the two theodolites are
collimated on each other and the azimuth scales are set to 0 and 180 deg, res-
pectively, making the two coordinate systems parallel. Collimating the first
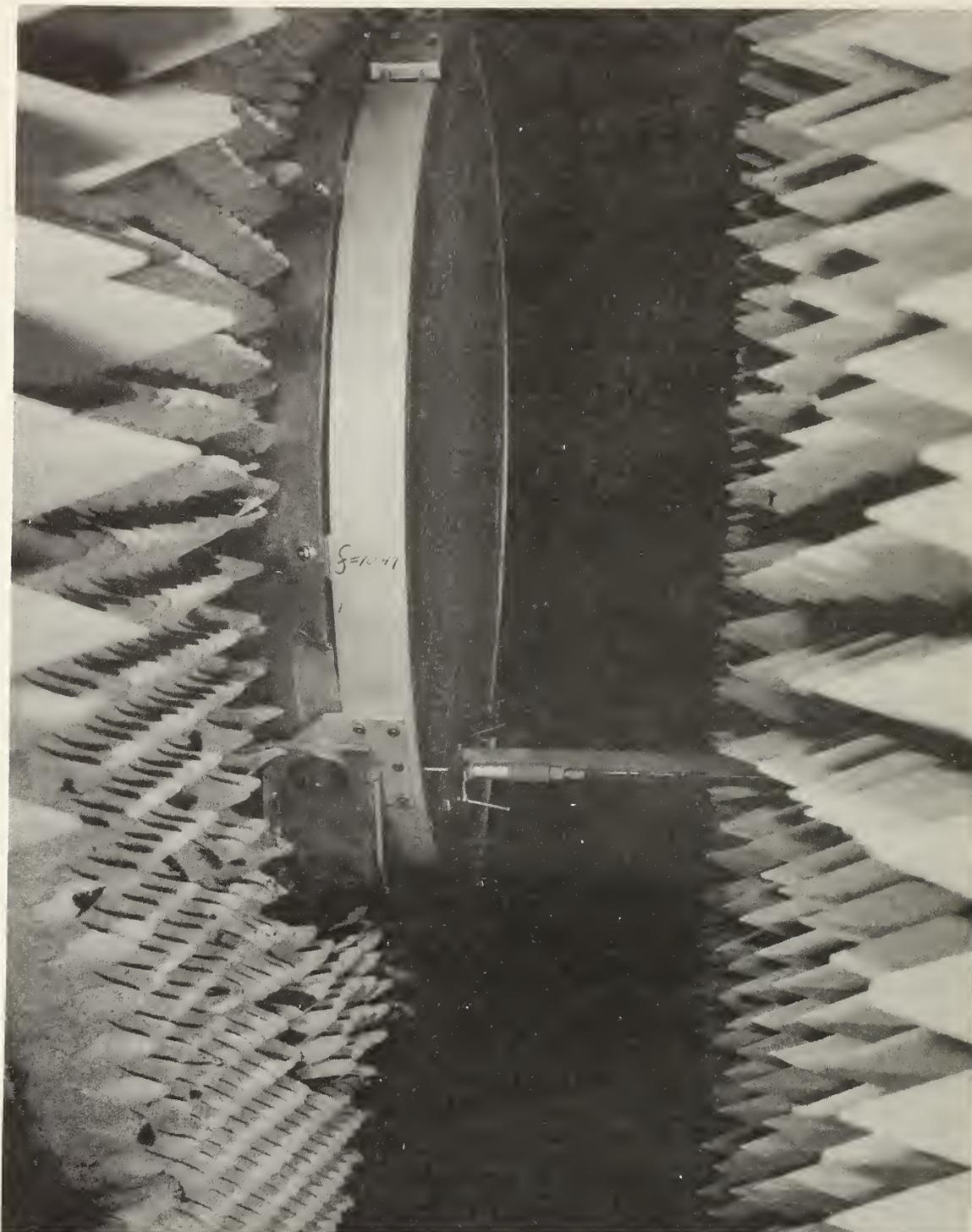
47

Figure 31. Micrometer used to align antenna mechanically to reference scan plane.
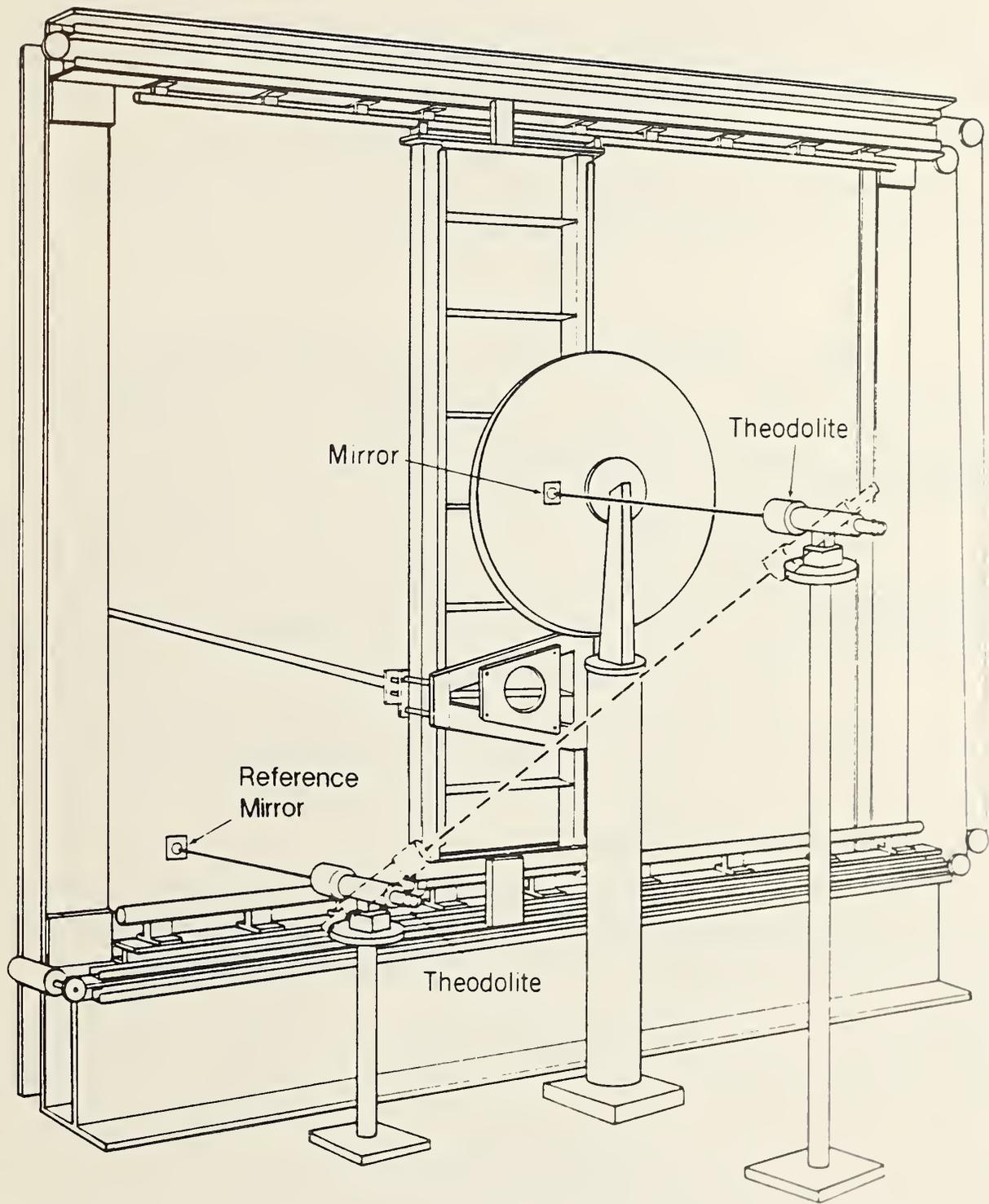
Figure 32. Dual theodolites used in optical antenna alignment.

49

on the reference mirror and setting the angles of both to the same value orients both theodolites normal to the reference mirror. The AUT can then be rotated to collimate its mirror on the second theodolite and hence align its z-axis parallel to the reference coordinate system. Similar techniques can then be used with the theodolite collimated on a second mirror (see fig. 30) as the AUT is rotated about its z-axis to complete the alignment.

Assuming that the collimation technique has been used, the estimates of uncertainty in the alignment are itemized in table 3.

Table 3. Estimates of uncertainty for antenna alignment.

Source of error	Alignment error (arc seconds)	
Definition of reference axes (from table 2)	15	
Collimation errors		
Two theodolites		5
To reference mirror		5
To antenna		5
Angle measurement		5
Alignment resolution		5
Root sum of squares (RSS)		19

5.5.1 Far-Field Angle Measurement

In the near-field measurements, angles to define directions for far-field patterns are not measured directly. Measured quantities are the x- and y-positions, and the amplitude and phase of the near fields at each of these positions. Through the Fourier transform the far-field spectrum, which is given as a function of the wave numbers k_x and k_y, is derived. Angles are then derived through the relations

$$k_x/k = \frac{\lambda \, (i_c - N_c/2)}{N_c \delta_x} = \cos E \, \sin A \qquad (24)$$

$$k_y/k = \frac{\lambda \, (i_r - N_r/2)}{N_r \delta_y} = \sin E. \qquad (25)$$

where i_c and N_c are the column index and number of near-field columns, with similar definitions for the row parameters i_r and N_r.

Angle errors are then related to errors in the dimensions of the scan lengths L_x and L_y, and wavelength; namely

$$\Delta A = \frac{1}{\cos E \cos A} \left(\frac{\Delta \lambda}{L_x} - \frac{\Delta L_x}{L_x^2} \right) \tag{26}$$

$$\Delta E = \frac{1}{\cos E} \left(\frac{\Delta \lambda}{L_y} - \frac{\Delta L_y}{L_y^2} \right), \tag{27}$$

where $L_x = N_c \delta_x$ and $L_y = N_r \delta_y$.

5.6 Measurement Errors Affecting Boresight Errors

There are certain errors in the amplitude and phase data that can cause errors in boresight. These errors produce an artificial offset in the far-field spectra that are independent of the alignment errors previously discussed. From analytical studies, computer simulation, and tests during near-field antenna measurements, the following have been identified as primary contributors:

1. z-position errors
2. Linear phase errors due to flexing of cables;
3. Phase errors due to receiver nonlinearity;
4. x- or y-position errors;
5. Truncation;
6. Multiple reflections, and
7. Phase drift during measurement due to temperature change.

The magnitude of each of these errors will depend on the particular measurement system, the frequency of operation, and the character of the AUT. For instance, if the AUT is a well-collimated antenna with the main beam along the z-axis, the near-field phase is essentially constant as a function of x and y. In this case, x-y position errors and receiver linearity will have little effect. If the beam is not well collimated, or if it is steered off axis, both of these will have a significant effect since the phase will change rapidly as the probe moves over the scan plane. In some cases, error

51

equations are available to estimate the magnitude of the beam alignment errors [16] and in other cases, special tests must be performed to identify their effect. One such test is to compare beam pointing results from two different measurements on the same antenna. In the two measurements, the antenna has been rotated about the z-axis by 180 deg and precisely aligned in each case. Other similar comparisons can identify individual errors. An example of results for such tests is summarized in table 4.

Table 4.   Estimates of uncertainty for beam pointing.

| Source of error | Beam pointing error (arc seconds) | |
	Narrow beam antenna	Broad or steered beam
z-position errors	20	100
Cable flexing or rotary joints	20	20
Receiver phase nonlinearity	20	50
x-y position errors	5	60
Truncation	10	30
Multiple reflections	10	60
phase drift	5	5
Antenna alignment (from table 3)	19	19
Estimated total uncertainty root sum square combination	43	146

6.   Development of Near-Field Swept-Frequency Measurement Techniques

6.1   Introduction

Swept-frequency measurements of the complete satellite system including transmitter, receiver, and the associated antennas are an important part of pre-launch testing of communication satellites. "Holes" in the frequency response of any part of the system cause degradation or loss of performance in some of the channels, and therefore reduce the value and usefulness of the satellite. Each part of the system is tested separately and the total system is also evaluated to detect any problems arising from system interactions. In the past, these measurements have been performed using far-field techniques. If near-field testing is to be used on these systems, methods must be

developed to provide equivalent information. In this section we will describe the development of such techniques and give sample results. Some aspects of the far-field testing are discussed first and establish a basis both for comparison and to define requirements.

6.2 Analysis

The potential amount of data required for complete frequency characterization of a satellite system is massive, and therefore some choice is always made to obtain a practical and yet adequate data subset. The total potential data set is viewed as a three-dimensional volume in figure 31 where the far-field angles are two dimensions, and frequency is the third. Covering the complete volume requires fine increments in all three dimensions. Testing time is prohibitive for such complete characterization, and therefore either the angular or frequency coverage must be reduced. The usual choice is complete patterns at a few (10-20) frequencies across the operating band, represented by the horizontal slices in figure 33. The patterns are then supplemented with continuous swept-frequency measurements at important or representative key angular locations as illustrated by the vertical lines. These locations are typically the peak of the beam where gain variation is obtained, and the edge of coverage where isolation between beams is measured. It is implicit that these limited tests represent typical performance at similar angular locations of the pattern, and therefore complete angular coverage is not necessary.

Swept near-field measurements yield results similar to the far-field tests, but measurements at one near-field point do not directly represent the frequency response in any one far-field direction. They require further analysis and interpretation and will be used as a guide and supplement to the complete near-field measurements at fixed frequencies. In the following, we will describe how they are used first to specify the required frequency increments and also to give an approximate far-field frequency response.

We begin with a hypothetical case based on three assumptions; it illustrates the desired information, the measured data, and the problems to be solved. (1) The pattern, gain, and polarization of the AUT are required only over a limited angular region in the far field. For the satellite antennas under consideration this is a region of approximately 20 deg in both azimuth
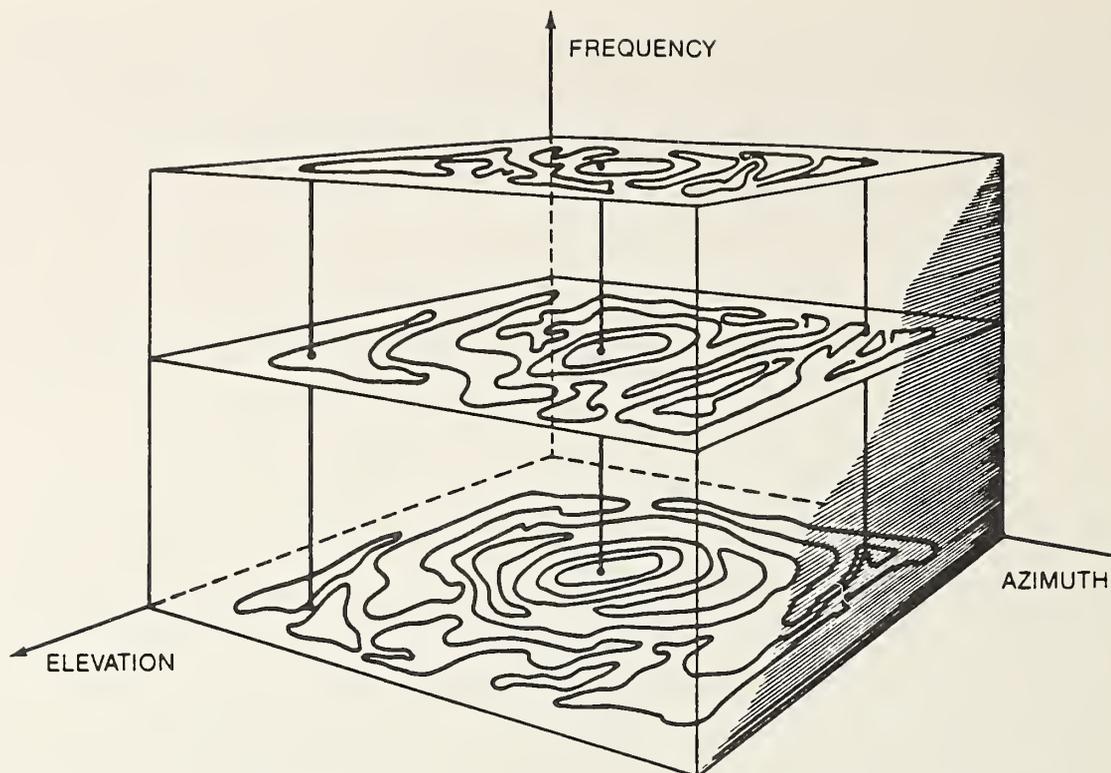
53

Figure 33. Schematic representing three-dimensional data volume.

and elevation. (2) Within this angular region of interest the far-field frequency response is required at a few (three to five) specific locations. The $\underline{K}$ values specifying these angular locations are denoted as $\underline{K}_i$. A sample of a typical swept measurement is shown in figure 34 where the peak gain of an antenna at $\underline{K} = \underline{0}$ has been measured over the operating frequency band. (3) At each of these locations the frequency response curves are accurately represented by stepped frequency measurements with increment $\Delta f(\underline{K}_i)$. In general, the required frequency increments may depend on the part of the pattern being measured; sidelobes and cross-polarization require smaller increments than the peak of the beam. In the example of figure 34, the smallest measured period is 350 MHz, and the corresponding $\Delta f(\underline{K}_i)$ is 175 MHz. The $\Delta f(\underline{K}_i)$ essentially define frequency sampling criteria for the far-field measurements and guarantee that, if measurements are made at increments of $\Delta f(\underline{K}_i)$ or less, the complete response can be reconstructed. The measured data at 175 MHz increments will not have the fine resolution of the curve in figure 34, but since we have determined a minimum period in the measured data, Fourier analysis will produce complete reconstruction. The
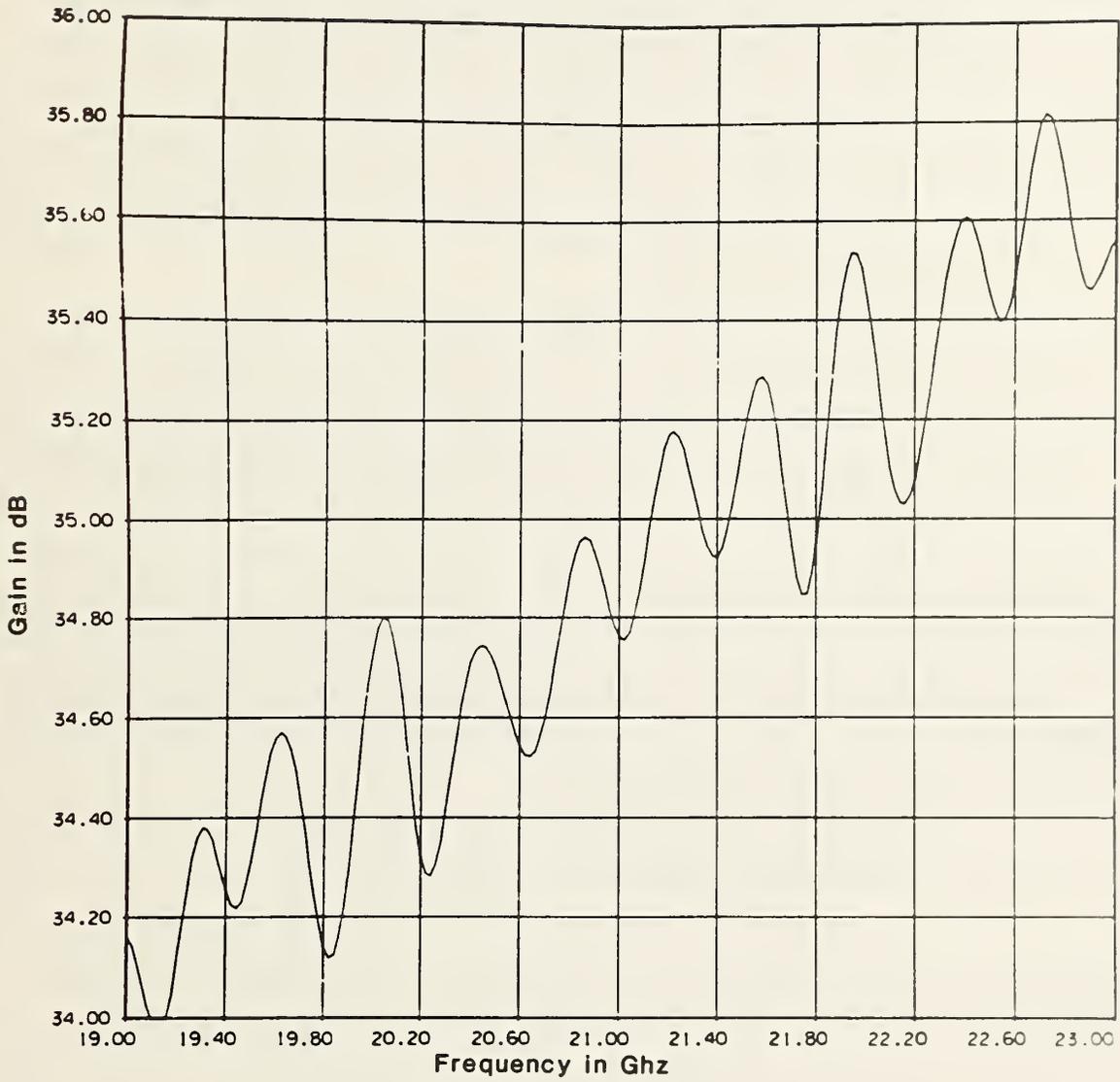
Figure 34.   Sample swept-gain results.

55

first two assumptions are realistic for the satellite antenna systems being measured and they also assist in a practical solution to the measurement problem. The third is not generally known; in fact it is one of the objects of the measurement, but once it is determined the remainder of the approach is straightforward.

The first assumption reduces the magnitude of the problem because it reduces the near-field data necessary to characterize the far field. As already noted for fixed frequency measurements, the size of the scan area is reduced and the data point spacing increased for these limited angular regions. Especially for the peak gain frequency data, only the near-field region where the amplitude is relatively large and the phase smoothly varying will make a significant contribution.

The second assumption means that there may be rapid frequency variations in wider angular regions or at selected locations within the angular region of interest. However, if these variations are not at any of the selected locations, they do not have to be considered in determining the minimum frequency sampling interval.

The third assumption is the key one. If by some means these frequency sampling intervals can be determined, the remaining measurements are routine. Given that the $\Delta f(\underline{K}_i)$ are known, complete near-field data at these frequency increments produce complete far-field parameters by the usual Fourier transform of each data set at a given frequency,

$$D'(\underline{K}, f_j) = \frac{e^{-i\gamma d}}{4\pi F'} \int \frac{b_0'(\underline{P}, f_j)}{a_0(f_j)} e^{-i\underline{K} \cdot \underline{P}} d\underline{P}. \tag{28}$$

For polarization information, similar data with a cross-polarized probe is necessary and requires similar processing.

$$D''(\underline{K}, f_j) = \frac{e^{-i\gamma d}}{4\pi F''} \int \frac{b_0''(\underline{P}, f_j)}{a_0(f_j)} e^{-i\underline{K} \cdot \underline{P}} d\underline{P}. \tag{29}$$

In the above,

$$f_j = f_0 + j\Delta f(\underline{K}_i), \tag{30}$$

where f_0 is specified.

56

Without knowing the frequency sampling criteria, many more near-field scans are required. This illustrates the importance of determining $\Delta f(\underline{K}_i)$ before making any near-field measurements. In a near-field system the far-field frequency response cannot be measured directly, and we must therefore develop equivalent tests and analysis to determine the frequency sampling criteria.

The test proposed and studied is one where swept-frequency measurements at very closely spaced frequency increments are performed at a few selected locations in the near field. The combinations of these data will have the same frequency sampling requirements as the far fields in the prescribed locations. If we determine the sampling requirements from the near-field data, the far-field requirements are therefore known.

The near-field swept-frequency tests are performed as illustrated schematically in figure 35. The generator and load ports are first connected together, the frequency is varied in very small increments, and the amplitude and phase are recorded at each frequency. These data serve as the reference curve that defines the variation of input signal and measurement system response. The generator is then connected to the AUT, the load to the probe, and the probe is placed at some point in the near field $\underline{P}_n$. The frequency is again varied over the same range, with the same increments, and again the amplitude and phase are recorded. The ratio of these two measurements is the near-field frequency response of the AUT/probe combination for that particular x,y,z probe position. A sample of one such measurement is shown in figure 36. Fourier analysis of this single swept measurement, as shown in figure 37, shows a pulse width of approximately 50 ns corresponding to a frequency sampling requirement of 20 MHz.

Before describing data analysis techniques further, we will consider the mechanisms that produce frequency variations in the antenna system and how these influence the choice of probe type and probe location for swept tests. There are a group of components that affect all far-field directions and, therefore, every near-field location equally. These include the electronics of the transmitter/receiver, the transmission lines between the electronics, and any switches, couplers, connectors, etc., common to all antenna elements. Frequency variation caused by these components are detected by placing the probe at any location.
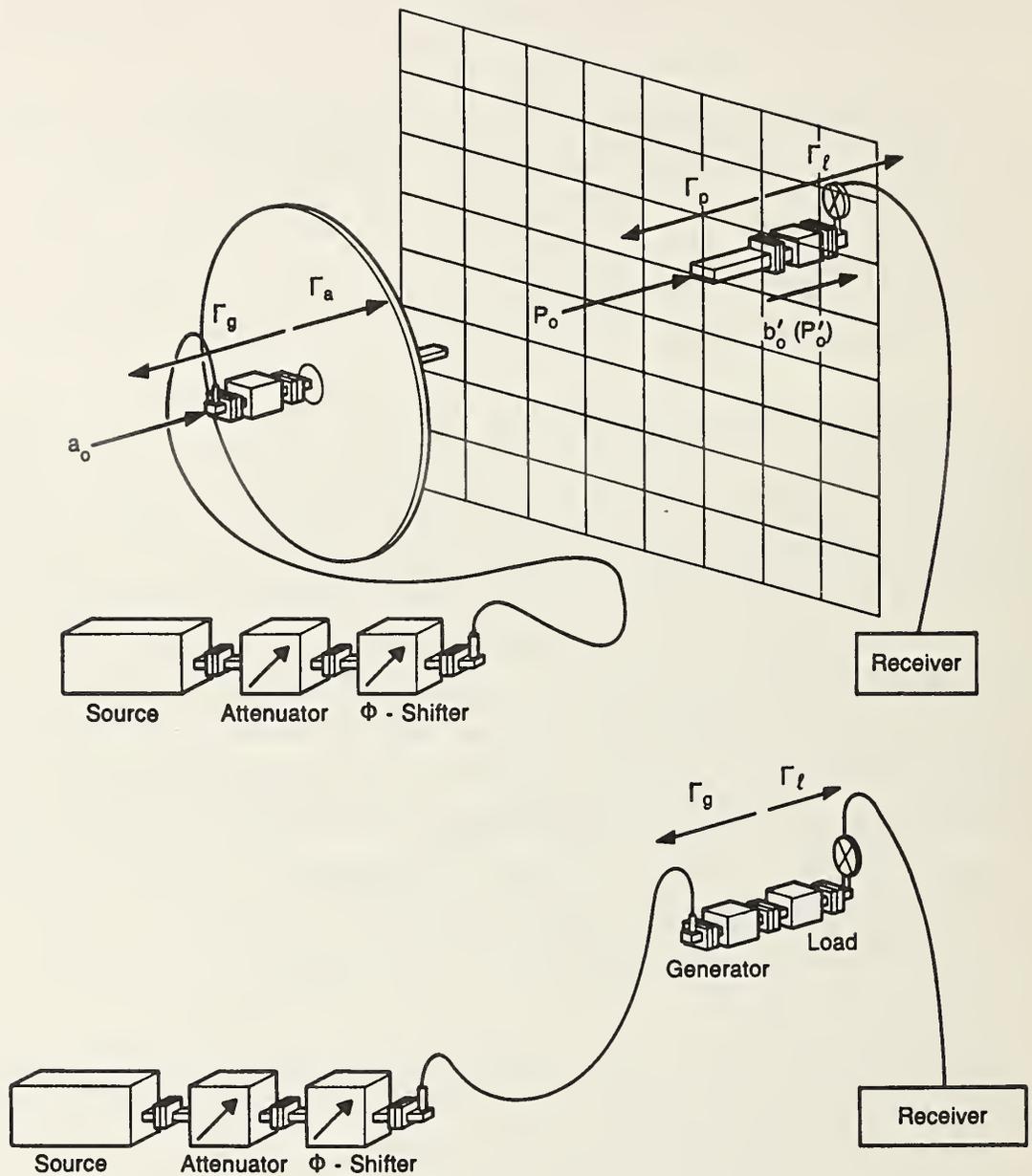
Figure 35. Schematic of two parts of swept near-field measurement illustrat-
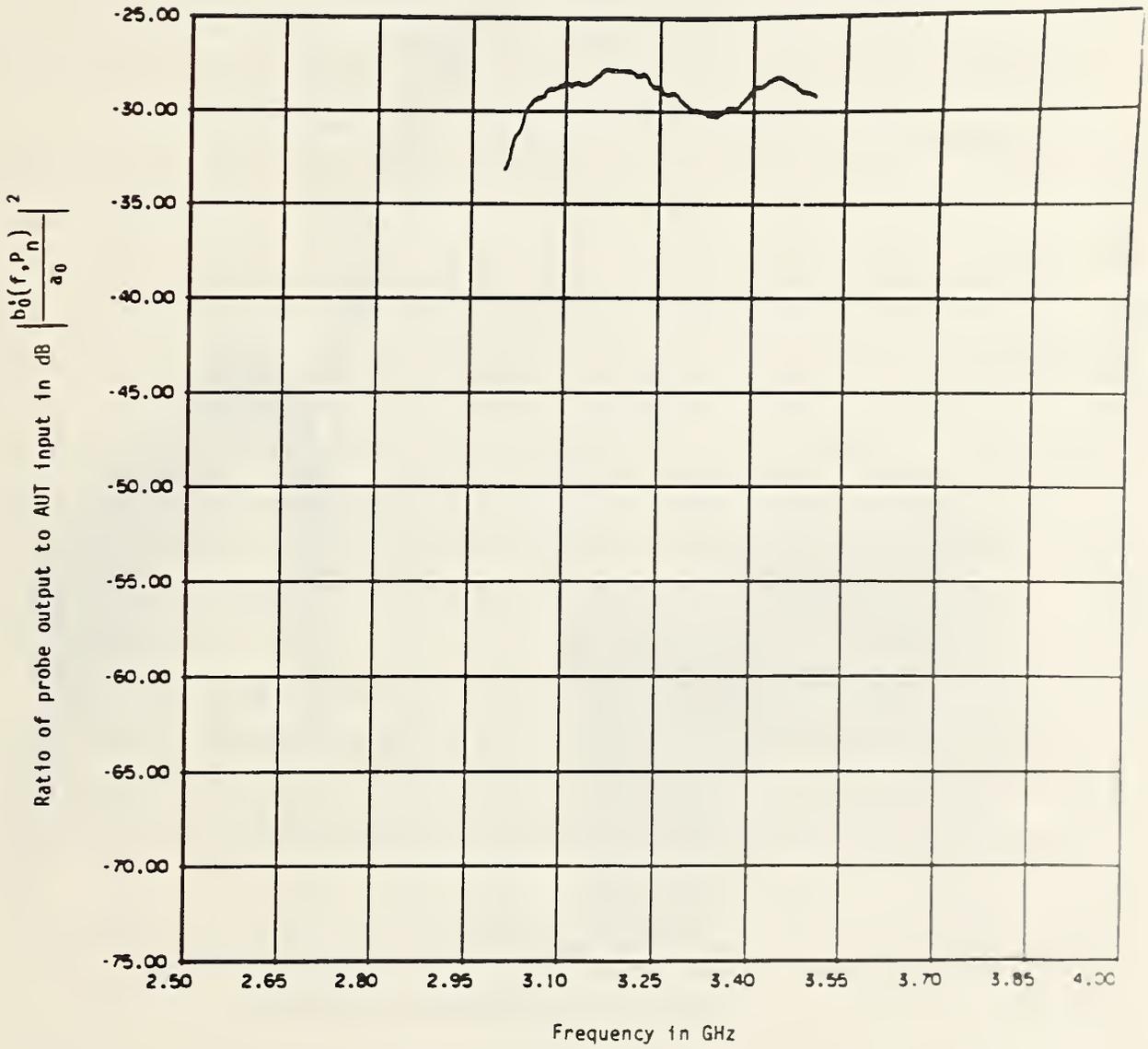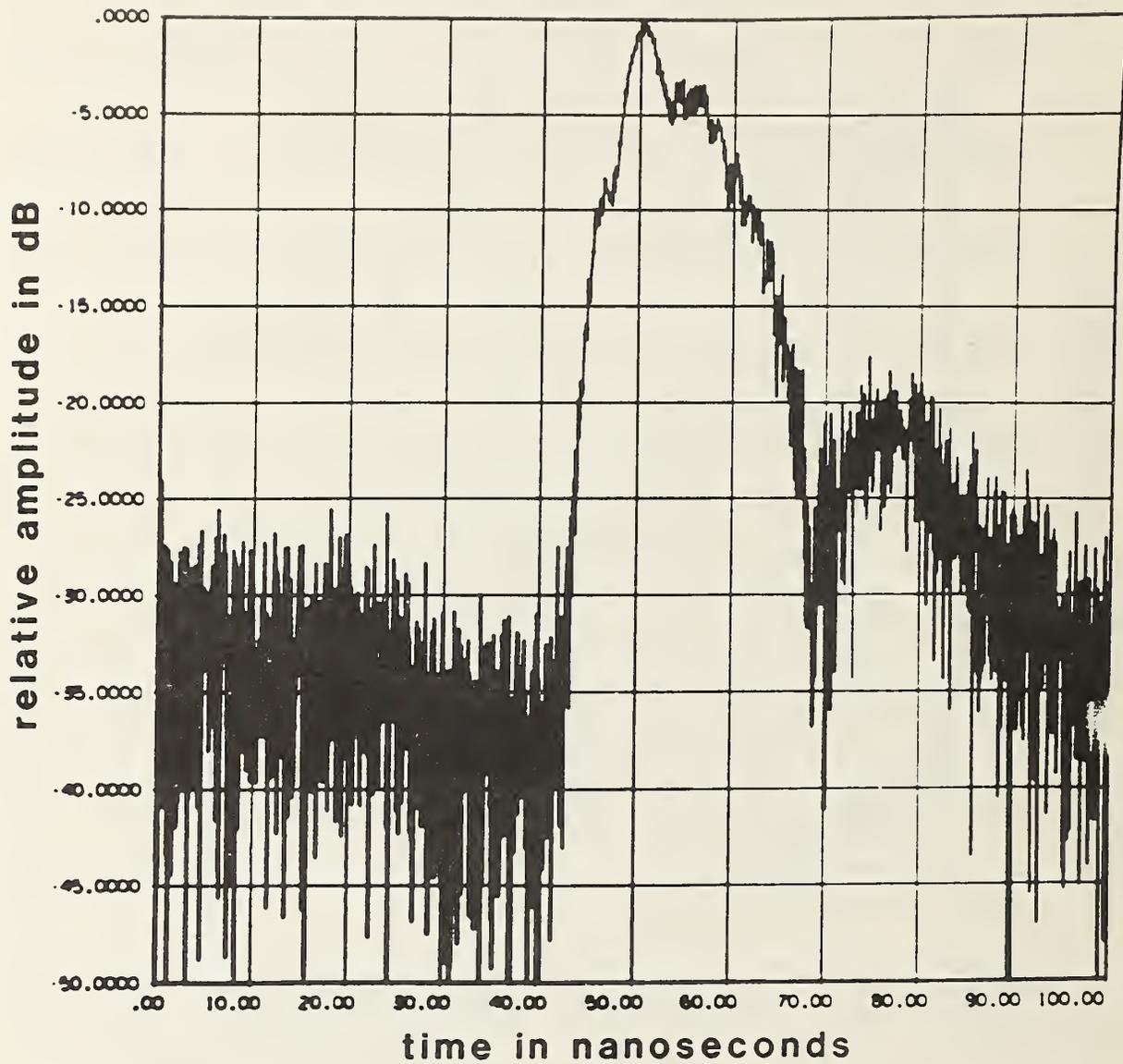ing generator-to-load and antenna-to-probe measurements.

Figure 36. Sample results from swept near-field measurements.

59

Figure 37. Time-domain representation of swept near-field measurement data.

If the feed or the antenna itself is composed of individual elements, there is another group of transmission lines, connectors, and possibly electronics associated with individual elements. In the case of a phased array, the probe would have to be near a particular element to detect the complete frequency characteristics of that individual element. If the probe is very close to the array surface, and not near the element, swept measurements will not detect its effect. If the probe is moved farther from the array, the effect of a single element becomes less, but the probe will "see" some effect. In the far field the effect of the single element is likewise smoothed out. The above all indicate that the probe should be placed at z-distances as far away as possible for swept-frequency tests within the constraints of the measurement facility.

If the feed of a reflector antenna is composed of individual elements, each element produces an approximate plane wave, and within the collimated region the probe responds to the combined effect of each feed element. In a particular direction in the far field one element may have a larger effect than the others, and this will not be apparent in the near-field data. Techniques will be described later to process the swept data in a way that tends to focus on a specific direction, and either emphasize the contribution of a particular feed element or reduce the effect of variations not associated with that direction.

Scattering from the reflector, the feed, and other structures produces frequency variations with minimum periods corresponding to the size or distance between structures. For a dimension ℓ in the radiating or scattering system, the corresponding period in the swept-frequency data is

for single reflection

$$\Delta f = \frac{c}{\ell} \tag{31}$$

or

for multiple reflections

$$\Delta f = \frac{c}{2\ell}, \tag{32}$$

where c is the velocity of light. An estimate of $\Delta f(\underline{K}_i)$ can therefore be based on mechanical dimensions.

Taking each of these factors into account, the following guidelines are established for the near-field swept-frequency tests.

A. The probe should have a relatively smooth frequency response over the measurement band since the measured frequency response is a combination of both system and probe characteristics.

B. The separation distance between the AUT and the probe should be as large as possible within the facility size constraints.

C. The probe pattern should be relatively constant over the angular region of interest. This will generally be required for the regular near-field tests.

D. Swept measurements are then taken at a few representative points in regions where the amplitude is the largest. This is generally the collimated region corresponding to the antenna's physical area for the main component data. Typical positions are along the two centerlines and in the region of the four quadrants. For the cross component, the field is often very low along the centerlines and the region of the four quadrants is better. Typically, a two-dimensional scan such as figure 38 is obtained to aid in choosing representative regions where the amplitude is significant.

There are two approaches for choosing the $\Delta f(\underline{K}_i)$ frequency increments. In the simplest, each individual swept measurement is analyzed separately to determine the required sampling increments. The minimum frequency increment from all of the measurements is used for all $\underline{K}_i$ directions. The second approach is suggested by the Fourier transform analysis of the near-field data in eq (28). The individual swept measurements are combined by the relationship

$$G'(f_j,\underline{K}_i) = \left| \sum_{n=1,N} \frac{b_0'(\underline{P}_{-n},f_j)}{a_0(f_j)} e^{-i\underline{K}_{-i}\cdot\underline{P}_{-}} \right|^2 , \tag{33}$$

where $G'(f_j,\underline{K}_i)$ is the approximate gain variation in the given direction. This produces a swept-frequency curve that corresponds to a particular location in the far field. In this processing, lower amplitude measurements are automatically given less weight, and frequency variations that are not phase
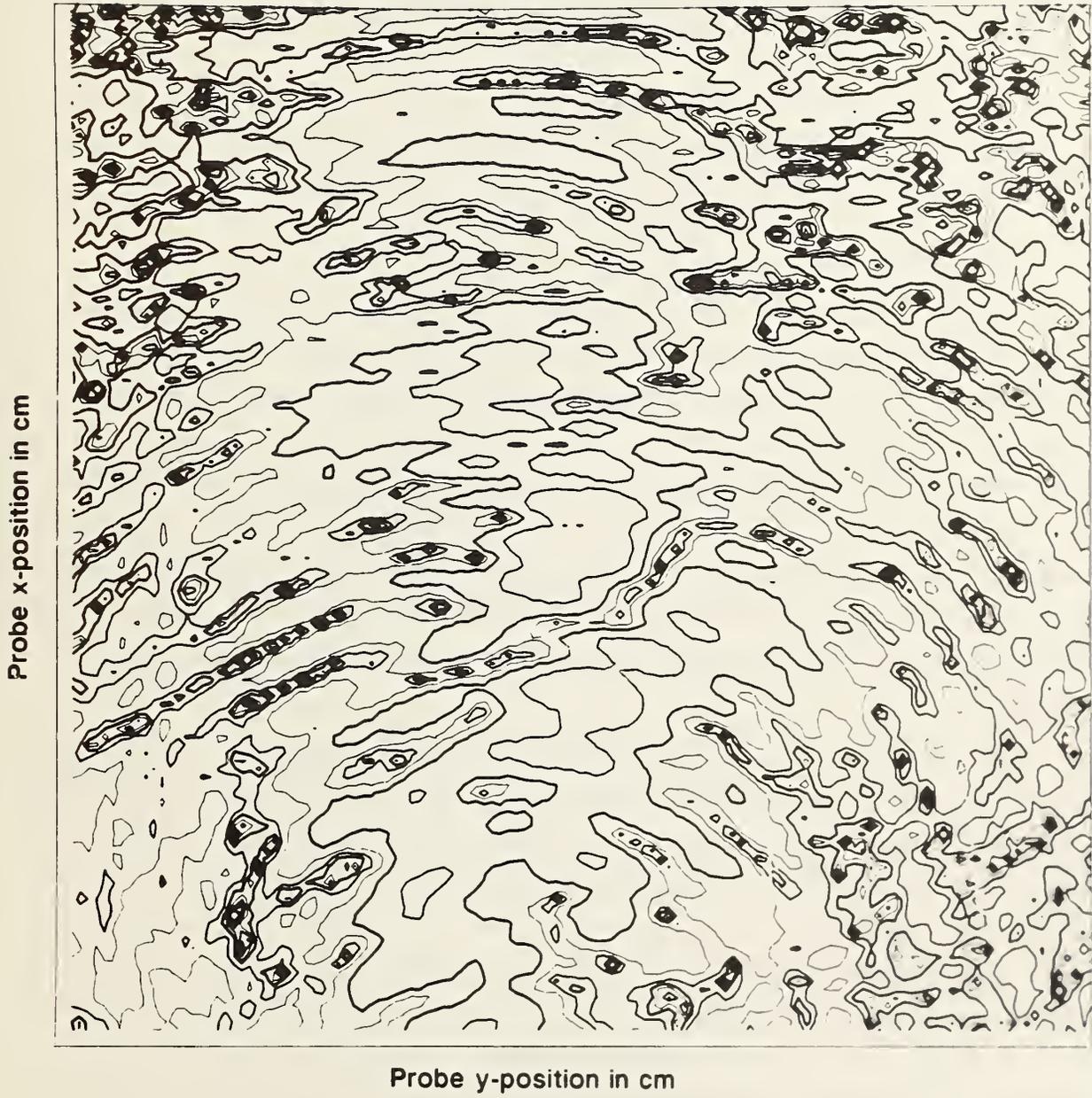
Probe x-position in cm

Probe y-position in cm

Figure 38.   Contour plot of near-field cross component data.

63

coherent at the different measurement points will tend to average out. As the number of swept measurements increases, the validity of this approach also increases. Experience and further study will indicate the most effective tradeoff between the number of measurement points and the accuracy of the results.

Figure 39 shows an example of combining swept data using eq (33). Preliminary results have been very promising. Further testing will be pursued during Phase II.

7. Specification of Hardware Requirements for Planar Near-Field Testing of Satellite Antenna Systems

7.1 Introduction

A typical near-field measurement system is shown schematically in figure 40. The specifications of the measurement system will be discussed in terms of the five subsystems: (1) the mechanical probe positioning system, sometimes referred to as the scanner; (2) the rf source that produces the stable measurement signal; (3) the receiver with any associated preamplifiers that converts the probe output signal to a digital record of the amplitude and phase; (4) the rf probe used to sample the radiated field, or in the case of a receiving antenna, to illuminate the test antenna, and (5) the computer that controls the measurement process and in some cases performs the numerical analysis.

There are two types of specifications for the measurement system. The first defines the requirements for any measurement on a given antenna system. Examples of these are the frequency coverage of the source and receiver, and the size of the scanner. The second type determines the accuracy of a given measurement, and these will receive the primary attention. The process for specifying the requirements of each of the sub-systems uses as input data the information about the antenna system being measured, the accuracy requirements, and the kinds of final results needed. For each of the final results, we then construct an error budget that allocates a portion of the error to each of the known sources of error. Using the equations developed from studies of the error sources [3], the subsystem specifications can be determined.
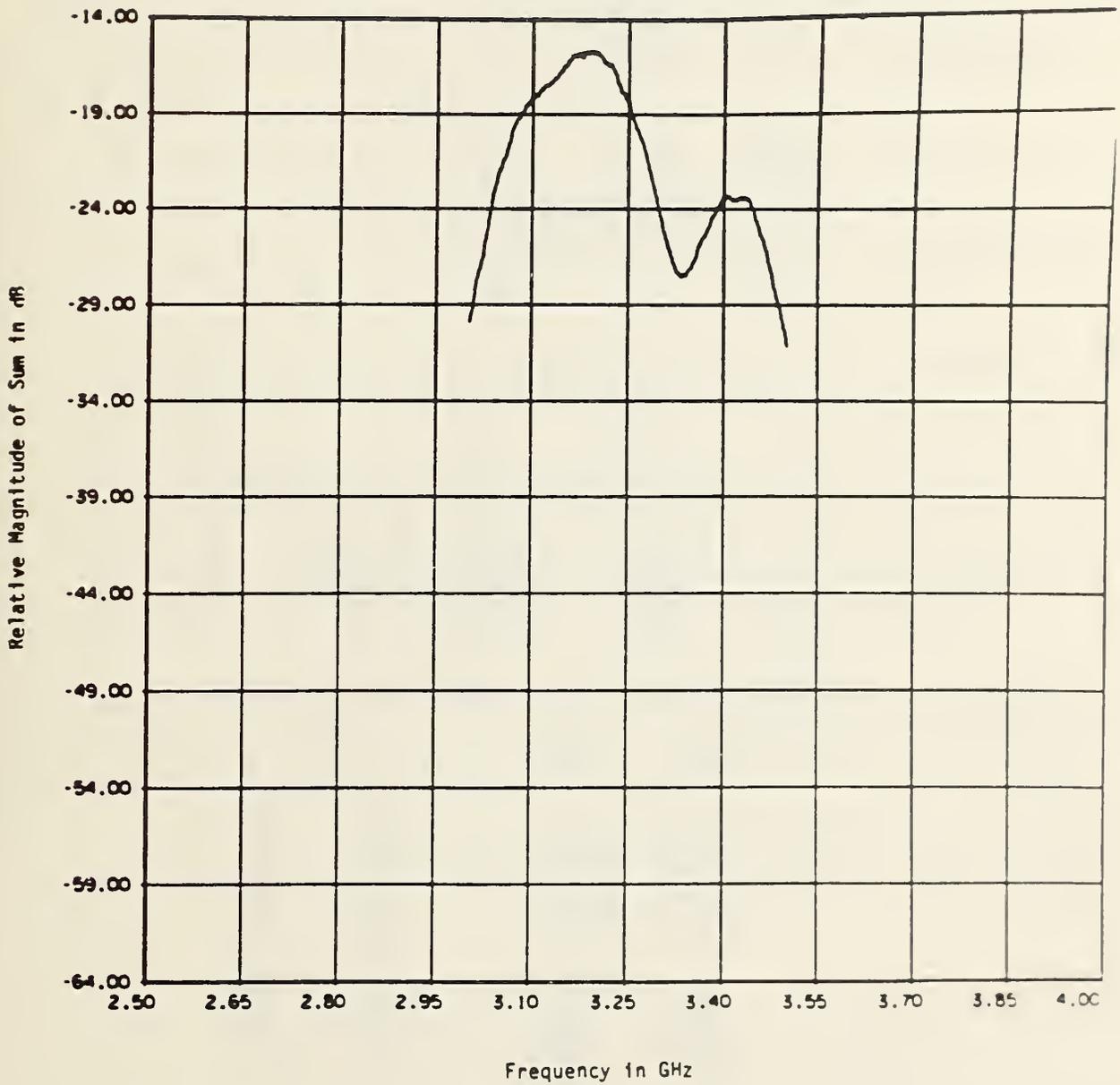
Figure 39. Combination of swept frequency curves for on-axis direction
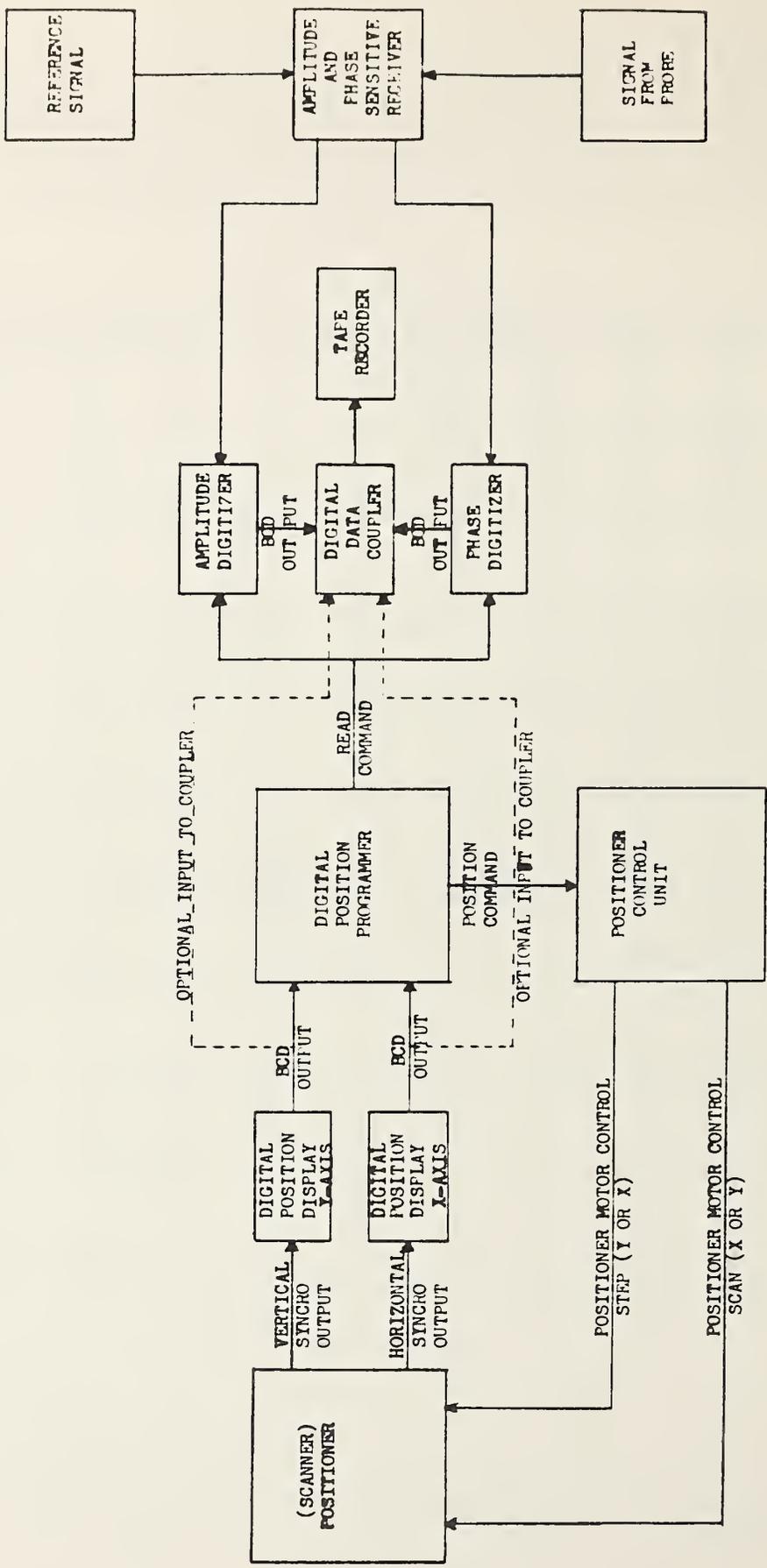response.

Figure 40. Schematic of near-field measurement system.

7.2 Antenna System Measurement and Accuracy Requirements

For this study, the antenna system considered is the Intelsat VI shown in figures 41 and 42. It is composed of offset reflector antennas operating in the frequency ranges of 3.4 to 4.2 and 5.8 to 6.6 GHz. These antennas are circularly polarized and produce shaped beams referred to as Hemi or Zone beams. The two-spot beam reflectors operate in the frequency band from 10.7 to 14.5 GHz. In addition, there are a cluster of global horns operating in the frequency range from 4.035 to 6.425 GHz.

While the measurement requirements differ somewhat for the different antenna systems, in general the following data are required:

A. peak gain at fixed frequencies in the center of each channel and at band edges;

B. relative patterns for both main and cross-polarized comonents over an angular region of ±10 deg from the subsatellite point;

C. EIRP measurements on the transmitting system and Saturating Flux Density measurements on the receiving system; and

D. swept measurements of peak gain, sidelobe levels, and polarization isolation at a few (5-6) Earth station locations within each beam.

The specified accuracy of the peak gain and power parameter measurements is 0.25 dB, while the specified accuracy of the sidelobe, cross-polarization, and isolation measurements is 0.75 dB.

Using the above measurement and accuracy requirements, table 5 lists the errors alloted to each of the individual sources affecting the peak gain result.
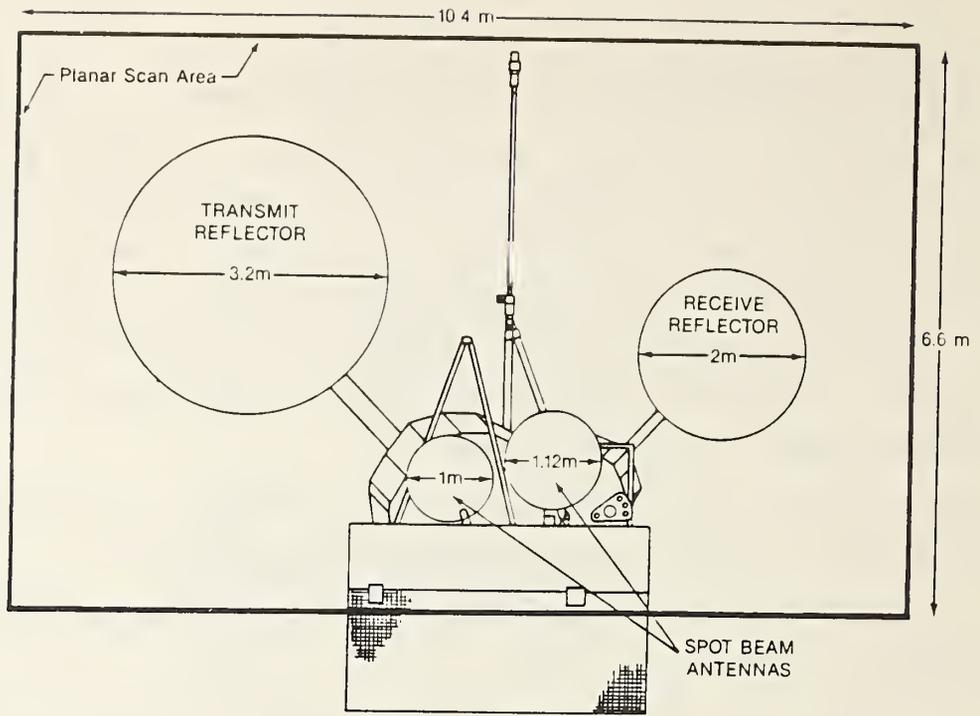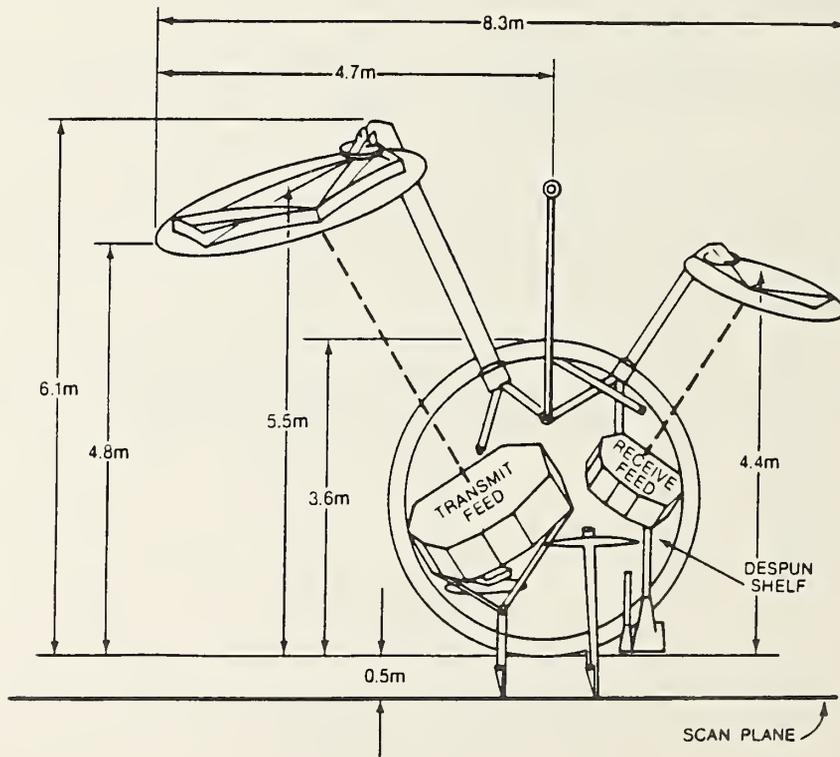
Figure 41. Schematic of Intelsat VI satellite.

Figure 42. Schematic of Intelsat VI satellite antennas.

Table 5. Error budget for peak gain measurements.

Error source	Error in dB
Probe relative pattern	0.00
Probe polarization ratio	0.00
*Probe gain	0.10
Probe alignment	0.02
*Normalization constant (or power measurement)	0.10
Impedance mismatch	0.05
AUT alignment	0.00
Aliasing error	0.00
Measurement area truncation	0.05
*Probe x-y position error	0.01
*Probe z-position error	0.01
Multiple reflections	0.15
*Receiver amplitude nonlinearity	0.01
*System phase errors	0.00
Receiver dynamic range	0.02
Room scattering	0.05
Leakage and crosstalk	0.05
Random errors in amp and phase	0.00
RSS combination (dB)	0.23

*See discussion below.

The magnitudes have been chosen to meet the requirement of 0.25 dB uncertainty and to reflect typical and realizable situations. The error sources are of two kinds. For those shown with an asterisk (*), there are error equations that give corresponding system specifications directly. For instance, the relationship between gain error and z-position error is

$$\Delta G < \frac{43}{\sqrt{\eta}} \left(\frac{\delta_z}{\lambda}\right)^2 \text{ (in dB)} \tag{34}$$

where η is the aperture efficiency, δ_z the magnitude of the z-position error, and λ the wavelength. Similar relations are available for the other parameters. These equations, along with a detailed discussion of the error analysis, are supplied in [16]. Using these relations, the allowable system uncertainties for peak gain are:

69

probe gain uncertainty   0.10 dB,

normalization constant measurement   0.10 dB,

probe (x,y)-position   0.01 λ,

probe z-position   0.01 λ,

receiver amplitude nonlinearity
  [16, eq. (63)] μ = 0.002, and

system phase error   2.0 deg.

For the remaining errors, tests must be performed on the actual AUT/Probe/Measurement system to estimate their magnitude. The truncation test has been discussed, and similar ones are described in the error analysis [14]. The magnitudes given in the above table are typical and should be realizable for the types of antennas to be tested. For the above errors, the tests should determine that the

truncation spectrum (similar to fig. 6)   < -45 dB,

peak-to-peak multiple reflections   < 0.15 dB, and

leakage and crosstalk   < -45 dB.

In table 6, the same error sources have been itemized for a -30 dB side-lobe in the main component pattern. The analytical error analysis has shown that when the errors vary sinusoidally in x and/or y, they have the most effect on the sidelobe region and that a particular period is associated with each direction in the far field. For instance, if the z-position error is of the form

$$\Delta z(x,y) = \delta_z \cos \left(\frac{2\pi y}{\tau}\right), \tag{35}$$

the sidelobes in the directions

$$\frac{k_y}{k} = \pm \frac{\lambda}{\tau} = \sin \text{ (elevation angle)} \tag{36}$$

will be in error, but in all other directions the error will be essentially zero.

70

Table 6. Error budget for -30 dB sidelobe measurement.

Error source	Error in dB
*Probe relative pattern	0.10
Probe polarization ratio	0.05
Probe gain	0.00
Probe alignment	0.20
Normalization constant (or power measurement)	0.00
Impedance mismatch	0.00
AUT alignment	0.00
Aliasing error	0.05
Measurement area truncation	0.15
*Probe x-, y-position error	0.06
*Probe z-position error	0.21
Multiple reflections	0.30
*Receiver amplitude nonlinearity	0.07
*System phase errors	0.23
Receiver dynamic range	0.20
Room scattering	0.05
Leakage and crosstalk	0.05
Random errors in amp and phase	0.00
RSS combination (dB)	0.56

*See discussion below table 5

The sidelobe region for the communication satellite antennas with aperture dimension a is bounded by the main beam with an approximate half-power beam width

$$\theta_B \approx \frac{\lambda}{10a} \text{ radians} \tag{37}$$

and the edge of Earth at approximately 10 deg off axis. The periods that will produce errors in this sidelobe region are then bounded by

$$6 \lambda < \tau < 10a. \tag{38}$$

This means that to satisfy the requirements for sidelobe accuracy, sinusoidal errors in amplitude, phase, or x-, y-, z-positions whose periods are within the range given by eq (38) must have magnitudes less than the following:

probe (x,y)-position   0.01 λ,

probe z-position   0.0005 λ,

receiver amplitude nonlinearity μ < 0.0004, and

system phase error   0.2 deg.

For the position errors, this implies a Fourier analysis of the position error data such as figures 25 or 27. The result of such an analysis on the z-position data is shown in figure 43. In this example, where f = 3 GHz, the periodic variation with τ = 100 cm affects the sidelobes in the directions where the elevation angle is 5.7 deg. The amplitude of 0.08 mm (corresponding to 0.0008 λ) is slightly larger than the required specifications. In such cases, the sidelobe error can be reduced by position error correction of the measured data. For example, since the position error can be measured with the laser to a resolution of at least 0.001 cm, and the primary effect of the error is on the phase, a simple correction that can be applied to the data is

$$\text{Phase correction} = \Delta\psi(x,y) = \underline{k}_0 \cdot \underline{\Delta r}(x,y) \tag{39}$$

where

$$\underline{k}_0 = \text{main beam propagation vector,}$$

$$\underline{\Delta r}(x,y) = \Delta x(x,y)\ \underline{e}_x + \Delta y(x,y)\ \underline{e}_y + \Delta z(x,y)\ \underline{e}_z. \tag{40}$$

With this correction the residual error is reduced to the specified level.

The requirement for measuring cross polarization ratio in the main beam region is an accuracy of 0.75 dB. While there is no stated restriction that this requirement applies to a nominal value for the polarization ratio, one must be assumed for practical application. For if the cross polarization approaches zero in some direction, the ratio approaches $-\infty$ and uncertainties of 0.75 dB cannot be maintained at these levels. We therefore assume that the nominal values are in the range of -30 to -35 dB. Table 7 shows an allocation of the error for these nominal values. The error equations employed are the same as for peak gain, since the angular region of interest is in the main beam region and the field component being measured is the main component for the probe. Since the signals are lower, scattering, multiple reflections, truncation, and dynamic range have a larger effect.
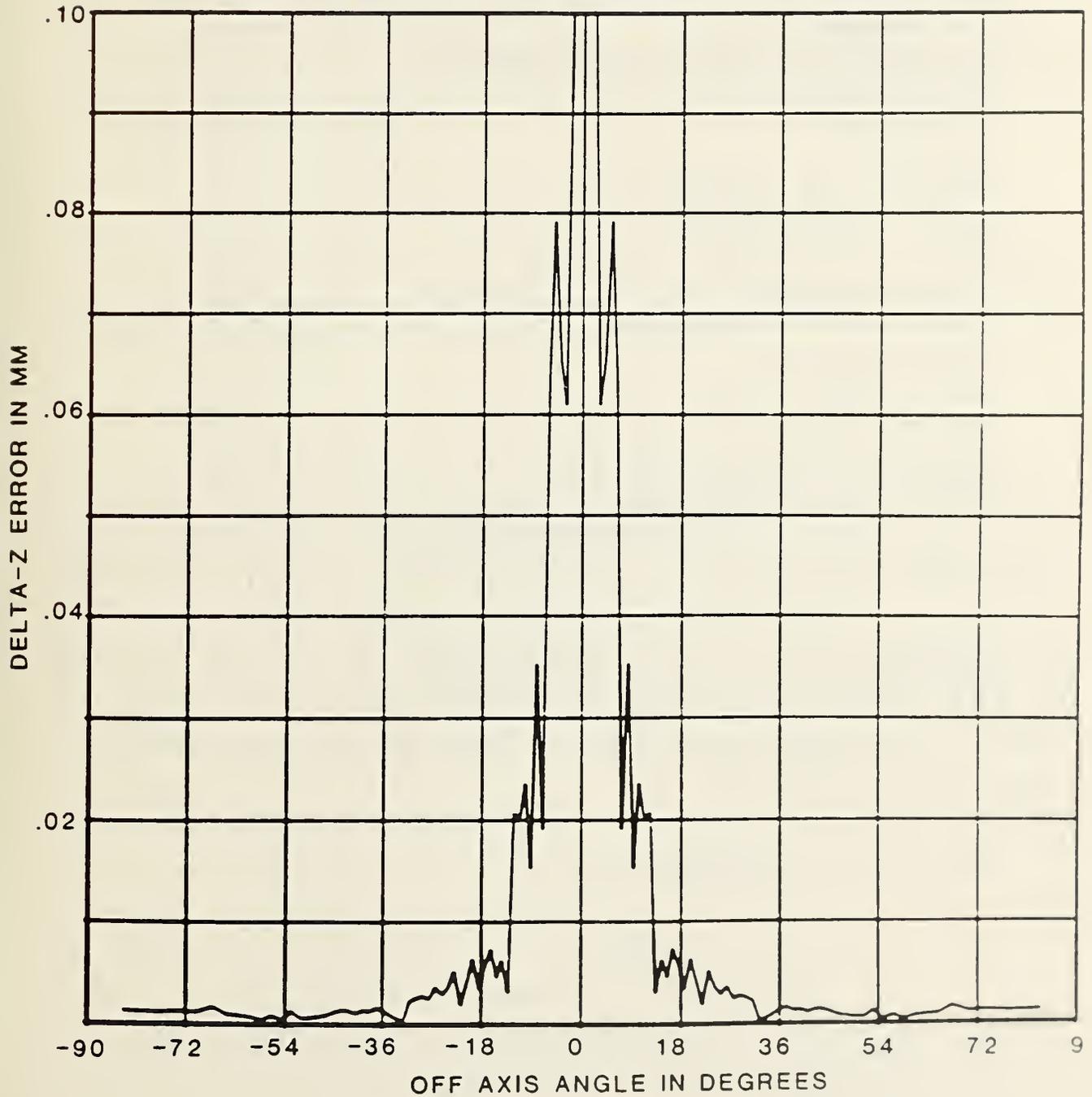
Figure 43. Fourier analysis of z-position error data.

Table 7. Error budget for cross polarization ratio in main beam.

Error source	Error in dB
Probe relative pattern	0.10
Probe polarization ratio	0.60
Probe gain	0.10
Probe alignment	0.02
Normalization constant (or power measurement)	0.20
Impedance mismatch	0.00
AUT alignment	0.00
Aliasing error	0.05
Measurement area truncation	0.20
Probe x- y-position error	0.01
Probe z-position error	0.01
Multiple reflections	0.25
Receiver amplitude nonlinearity	0.01
System phase errors	0.00
Receiver dynamic range	0.20
Room scattering	0.10
Leakage and crosstalk	0.10
Random errors in amp and phase	0.05
RSS combination (dB)	0.76

The uncertainty in the axial ratio and tilt angle of the probe used to measure the cross component also contributes to the error, and has been included in table 7. From the error analysis [16, eq (37)], the relationship between probe errors and AUT results is

$$\Delta AR_t(\underline{K}) = \text{axial ratio error in dB}$$

$$= \left| AR_t(\underline{K})e^{i2\tau_t} + AR_{s''}(\underline{K})e^{-i2\tau_{s''}} - AR_{s''E}(\underline{K})e^{-i2\tau_{s''\varepsilon}} \right| - AR_t(\underline{K})$$

where

$$AR = \text{axial ratio in dB,}$$
$$\tau = \text{tilt angle,}$$
$$t = \text{AUT parameters,}$$
$$s'' = \text{actual probe parameters, and}$$
$$s''_\varepsilon = \text{probe parameters used.}$$

For the 0.75 dB requirement, the probe parameters must be known to the following uncertainties:

probe axial ratio error < 0.05 dB, and

probe tilt angle error < 20.0 deg.

Using the combination of system specifications from the gain, sidelobe, and polarization ratio tables, we now can give the requirements for each part of the measurement system.

7.3 Specification for Antenna Measurement System

In tables 8 through 10, specifications are given for the scanner, the receiver, and the probe. The tables also identify the critical antenna measurements that determine the accuracy requirements.

Table 8. Mechanical probe positioner/scanner specifications.

Parameter	Critical antenna measurement	Specification
Size	Angular coverage	$L_x > a_x + 2d \tan \theta_x$ $L_y > a_y + 2d \tan \theta_y$
Size	Truncation error in: Sidelobes Cross polarization	 * < 0.15 dB error * < 0.15 dB error
x-position	Sidelobe	$\Delta_x < 0.01 \lambda$
y-position	Sidelobe	$\Delta_y < 0.01 \lambda$
z-position	Sidelobe	$\delta_z < 0.01 \lambda$
Scan plane stability	Boresight	Tilt change < 3 arc sec

d   = separation distance between probe and AUT

L_x, L_y = scan length in x-, y-directions

a_x, a_y = antenna aperture size in x-, y-directions

θ_x, θ_y = angular region of interest in x-, y-directions

$\Delta_x, \Delta_y, \Delta_z$ = position errors in x-, y-, z-directions

*Verify by test on actual antenna.

75

Table 9. Receiver specifications.

Parameter	Critical antenna measurement	Specification
Dynamic range	Sidelobe Cross polarization	* 40 dB * 40 dB
Amplitude linearity		
Nonperiodic	Gain	$\mu \leqslant 0.002$
Periodic	Sidelobe	$\mu(\underline{K}) \leqslant 0.0004$
Phase linearity		
Linear error (x,y)	Boresight	$\Delta\psi < 2^0/a_x, a_y$
Nonperiodic (x,y)	Gain	$\Delta\psi < 2$ deg
Periodic (x,y)	Sidelobe	$\Delta\psi(\tau) < 0.2$ deg

μ = receiver nonlinearity (see [16, eq (63)] for definition)

τ = period for sinusoidal errors

$\Delta\psi$ = receiver phase error

*Verify by test that dynamic range effect on results is within bounds of tables 5-7.

Table 10. Probe specifications.

Parameter	Critical antenna measurement	Specification
Gain	Gain	$\Delta G_p < 0.10$ dB
Pattern	Sidelobe	< 0.10 dB
Axial ratio	Polarization ratio	$\Delta AR \leqslant 0.05$ dB
Tilt angle	Polarization ratio	$\Delta T \leqslant 20$ degrees

ΔG_p = probe gain error

ΔAR = probe axial ratio error

ΔT = probe tilt angle error

This completes the summary of system specification. Although it applies to the specific antenna systems under study, the same process can be applied to any type of measurement requirements.

8. Summary

This report, along with Part 1 [1], completes the final report for Phase I on the Development of Near-Field Test Procedures for Communication Satellite Antennas. In this part, scan area and data point spacing requirements were analyzed to verify that the required parameters could be obtained and that techniques to determine the scan parameters were available. The results of both analysis and simulation demonstrate that the satellite antenna requirements can be met with near-field scanning.

A study of diagnostic techniques that would use either direct near-field data or various methods of processing to enhance the location of antenna anomalies was made. Phase data tends to be the most sensitive, and transformation closer to the antenna can give better resolution, but care must be exercised where evanescent modes are involved.

Techniques for the accurate alignment of the antenna to the mechanical scan plane were described, and estimates for the uncertainty of boresight measurement were derived.

Swept near-field techniques to define the required frequency spacing of complete near-field scans were developed. These swept measurements can possibly give estimates of far-field frequency performance, but this will require further development and verification.

Finally, the various parts of the study were combined, along with past error analysis studies to derive the system specifications for satellite antenna testing. These system specifications were developed using the required accuracy statements on far-field ranges. It was found that the system requirements are achievable with current mechanical and electronic equipment.

9. References

[1] Newell, A. C.; Repjar, A. G. Development of near-field test procedures for communication satellite antennas, Phase I, Part 1. Nat. Bur. Stand. (U.S.) NBSIR 85-3031; 1985 September.

[2] Newell, A. C.; Crawford, M. L. Planar near-field measurements on high performance array antennas. Nat. Bur. Stand. (U.S.) NBSIR 74-380; 1974 July.

[3] Yaghjian, A. D. Upper-bound errors in far-field antenna parameters
     determined from planar near-field measurements, Part 1: Analysis. Nat.
     Bur. Stand. (U.S.) Tech. Note 667; 1975.

[4] Grimm, K. R.; Hoffman, J. B.; Newell, A. C.; Francis, M. H. Final
     report: results of near-field probe scanning tests for ultralow sidelobe
     arrays, TSC-W41-406-kks. Technology Service Corporation Report; 1986
     May.

[5] Kefauver, N.; Cencich, T.; Osborn, J.; Osmanski, J. T. Final report:
     near-field testing of the 5-meter model of the tetrahedral truss
     antenna. NASA Contract Report 178147; 1986 August.

[6] Newell, A. C.; Stubenrauch, C. F. Effect of random errors in planar
     near-field measurements. IEEE Trans. Antennas Propagat., Special Issue
     on Near-Field Scanning Techniques; 1988 June.

[7] Repjar, A. G.; Kremer, D. P. Accurate evaluation of a millimeter wave
     compact range using planar near-field scanning. IEEE Trans. on Ant. and
     Prop. AP-30(3); 1982 May.

[8] Kerns, D. M. Plane-wave scattering-matrix theory of antennas and
     antenna-antenna interactions. Nat. Bur. Stand. (U.S.) Monogr. 162; 1981
     June. 162 p.

[9] Hamada, S.; Yeh, Y. Computer reconstruction of near-zone field from
     given far-zone data of two-dimensional objects. IEEE Trans. Antennas
     Propagat. AP-25: 304-311; 1977 May.

[10] Hamada, S.; Ingerson, P. G.; Rush, W. V. T. Reflector radiation pattern
     from planar near-field measurements of array feed. IEEE Trans. Antennas
     Propagat. AP-28: 436-442; 1980 July.

[11] Newell, A. C. Nat. Bur. Stand. (U.S.), private communication, 1985.

[12] Mayer, C. E.; Davis, J. H.; Peters, W. L. III; Vogel, W. J. A holo-
     graphic surface measurement of the Texas 4.9-m antenna at 86 GHz. IEEE
     Trans. Instrum. Meas. IM-32: 102-109; 1983 March.

[13] Godwin, M. P.; Whitaker, A. J. T.; Bennett, J. C.; Anderson, A. P.
     Microwave diagnostics of the Chilbolton 25M antenna using the OTS satel-
     lite. IEEE Conf. Pub. 195, Antennas and Propagation, Part I: Antennas.
     1981 April; London, England. 232-235.

[14] Bennett, J. C.; Anderson, A. P.; McInnes, P. A.; Whitaker, A. J. T.
     Microwave holographic metrology of large reflector antennas. IEEE
     Trans. Antennas Propagat. AP-24: 295-303; 1976 May.

[15] Bird, T. S. Contoured-beam synthesis for array-fed reflector antennas
     by field correlation. IEE Proc. 129(H): 293-298; 1982 December.

[16] Newell, A. C. Error analysis techniques for planar near-field measure-
     ments. IEEE Trans. Antennas Propagat., Special Issue on Near-Field
     Scanning Techniques; 1988 June.

U.S. DEPT. OF COMM. **BIBLIOGRAPHIC DATA** **SHEET** *(See instructions)*	1. PUBLICATION OR REPORT NO. NBSIR 87-3081	2. Performing Organ. Report No.	3. Publication Date August 1988

4. TITLE AND SUBTITLE

Development of Near-Field Test Procedures for Communication
Satellite Antennas Phase I, Part 2

5. AUTHOR(S)
Allen C. Newell

6. PERFORMING ORGANIZATION *(If joint or other than NBS, see instructions)* **NATIONAL BUREAU OF STANDARDS** **DEPARTMENT OF COMMERCE** **WASHINGTON, D.C. 20234**	7. Contract/Grant No.
	8. Type of Report & Period Covered

9. SPONSORING ORGANIZATION NAME AND COMPLETE ADDRESS *(Street, City, State, ZIP)*

10. SUPPLEMENTARY NOTES

☐ Document describes a computer program; SF-185, FIPS Software Summary, is attached.

11. ABSTRACT *(A 200-word or less factual summary of most significant information. If document includes a significant bibliography or literature survey, mention it here)*

The purpose of this program is to define and further develop the capabilities of near-field antenna test techniques, specifically for the requirements associated with the development and verification testing of reconfigurable, multibeam, frequency reuse, commercial satellite antennas. This report, Phase I, Part 2, focuses on the planar near-field measurement method and covers the determination of sampling criteria and scan limits, development of diagnostic and design assist methods, development of beam alignment techniques, development of swept-frequency equivalent tests, and specification of hardware requirements for the measurement system. Phase I, Part 1, a previous report, gave a general survey, definition, and description of near-field and compact range measurement methods as they apply to satellite antenna systems testing. Each of these methods was evaluated to determine how well they meet the measurement requirements. Included for each technique was a summary of the measurement method, discussions on probe correction and data processing, measurement hardware considerations, a results available section, and measurement accuracy and range certification considerations. The basis for the choice of the best measurement technique was established with the planar near-field measurement method receiving the best score for the directive antennas considered. It is for this reason that the planar near-field method is the focus of this report.

12. KEY WORDS *(Six to twelve entries; alphabetical order; capitalize only proper names; and separate key words by semicolons)*

antenna alignment; antenna boresight measurements; antenna diagnostics; antenna measurements; antennas; near-field measurements; near-field testing; planar near-field scanning; satellite antennas; swept-frequency measurements

13. AVAILABILITY ☒ Unlimited ☐ For Official Distribution. Do Not Release to NTIS ☐ Order From Superintendent of Documents, U.S. Government Printing Office, Washington, D.C. 20402. ☒ Order From National Technical Information Service (NTIS), Springfield, VA. 22161	14. NO. OF PRINTED PAGES 84
	15. Price